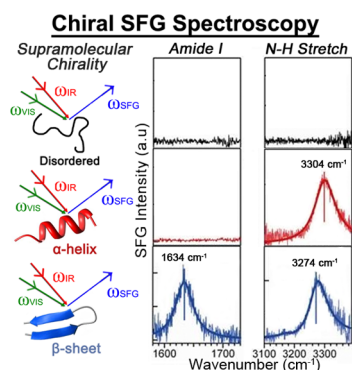# CHEMICAL REVIEWS

Biological Macromolecules at Interfaces Probed by Chiral Vibrational Sum Frequency Generation Spectroscopy

Elsa C. Y. Yan,* Li Fu, Zhuguang Wang, and Wei Liu

Department of Chemistry, Yale University, 225 Prospect Street, New Haven, Connecticut 06520, United States

Chiral SFG Spectroscopy

CONTENTS

1. INTRODUCTION

A fundamental understanding of chiral biomacromolecules at aqueous interfaces is critical to studying a host of important phenomena in modern biology, chemistry, and medicine. Examples of these phenomena include signal transduction and molecular transport across cellular membranes, immunological defense, drug delivery to target cells, rational design of functional materials, fabrication of molecular devices and biosensors, heterogeneous biocatalytic and enantioselective biochemical reactions, as well as the origin of life and its sustainability on inorganic substrates, such as aerosols and clay particles. Many biologically relevant molecules, such as sugars, nucleic acids, and amino acids have inherent chiral centers. These molecules polymerize into polysaccharides, DNAs and RNAs, as well as proteins, which can fold into chiral secondary, tertiary, and higher-ordered structures. These chiral structures are crucial to biological functions. They have also inspired
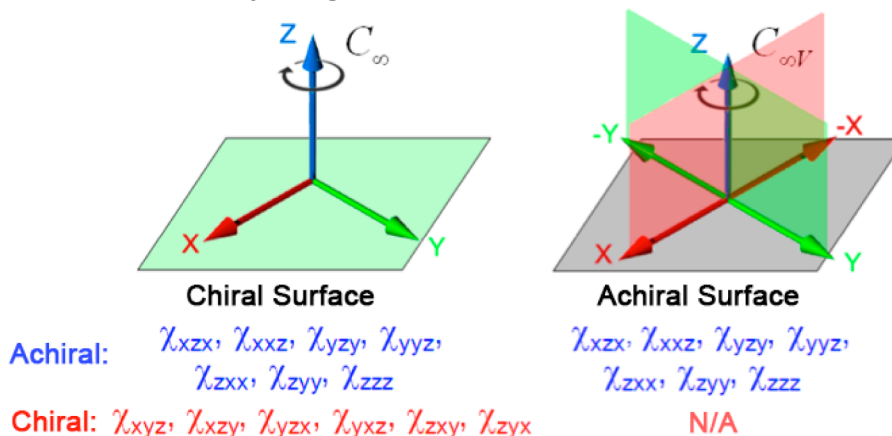
Figure 1. Symmetry of achiral ($C_{\infty V}$) and chiral surfaces (C_∞). The nonzero susceptibility elements of achiral surfaces (blue) and additional nonzero susceptibility elements of chiral surfaces (red). Zero susceptibility elements are crossed out.

designs of an array of biomimetic molecules, including β-peptides[1,2] and peptoids,[3] to assemble bioactive materials and to modulate biological processes. Owing to their great relevance in biomedical sciences, it is important to effectually characterize these native and synthetic chiral entities. However, there is a dearth of effective methods for the characterization and control of natural as well as artificial chiral macromolecules at interfaces as a result of the lack of effective surface-specific and chiral-selective techniques. Recent developments in chiral sum frequency generation (SFG) spectroscopy have offered new tools and opportunities in this broad and important field. This article reviews these developments for probing biomacromolecules at interfaces during the past decade.

This article focuses on the application of chiral vibrational SFG spectroscopy for characterizations of biomacromolecular structures at interfaces. Hence, this article will not discuss the applications of SFG methods in the studies of chiral bulk solution and bulk liquid,[4−8] or the applications of conventional (achiral) SFG in the studies of biologically relevant synthetic macromolecules,[9,10] proteins,[11−14] and other native biomacromolecules.[15] Detailed descriptions of SFG theory[16−22] and chiral SFG theory[23,24] for surface studies and application of other nonlinear methods, e.g., second harmonic generation, in probing molecular chirality[25,26] will also be excluded. Moreover, other related topics that have been recently summarized and discussed in review papers, such as theoretical approach to analyzing SFG spectra,[22] application of conventional (achiral) vibrational SFG spectroscopy for studying molecular structures and orientations at interfaces,[17,18,27−37] SFG studies of interfacial water structures,[19,38−41] and ultrafast vibrational dynamics probed by SFG,[42,43] will not be discussed here.

Instead, focus will be placed on the experimental and theoretical developments of chiral vibrational SFG spectroscopy and its applications in probing biomacromolecules at interfaces during the past decade. The theoretical basis for the surface specificity and chiral selectivity of vibrational SFG spectroscopy (section 2) will be introduced first, followed by a discussion on the design of SFG spectrometer for studying

biological systems (section 3). Then, a summary of experimental work using the chiral SFG method for characterization of the structures (section 4) and orientations (section 5) of native biomacromolecules as well as the kinetics of their conformational changes at interfaces (section 6) will be provided. One of the major challenges in analyzing biomacromolecular structures and orientations is the lack of knowledge about the molecular SFG response of biomacromolecules, i.e., the hyperpolarizability of biomacromolecules, which is generally difficult to calculate due to the size and complexity of biomacromolecules. This article will also review approaches in calculating hyperpolarizability of biomacromolecules (section 7). Finally, current challenges and a future outlook in the developments and applications of chiral vibrational SFG spectroscopy will be presented (section 8).

2. THEORETICAL BACKGROUND OF CHIRAL SFG

This section provides a theoretical basis for considering SFG as a surface-specific, chiral-sensitive vibrational spectroscopy. The general principle of SFG will be discussed. Then, a theory of chiral SFG will be presented, which was first formulated in detail by the Simpson group.[23,44]

2.1. General Principles of SFG

The general principle of SFG will be described here. More rigorous theoretical treatment is available in excellent review papers and books.[16−22] Vibrational SFG Spectroscopy is a second-order nonlinear optical technique, which uses two pulsed laser sources, one at infrared (IR) frequency (ω_{IR}) and the other at visible frequency (ω_{VIS}). When these two beams are made to spatially and temporally overlap at surfaces, a second order nonlinear optical process producing polarization at the sum frequency ($\omega_{IR} + \omega_{Vis}$) can be induced to generate SFG signals. The electric field of SFG signals, E_{SFG}, is related to the electric field of the two incident laser beams, E_{VIS} and E_{IR}, and the second-order susceptibility tensor, $\chi^{(2)}$, as described below
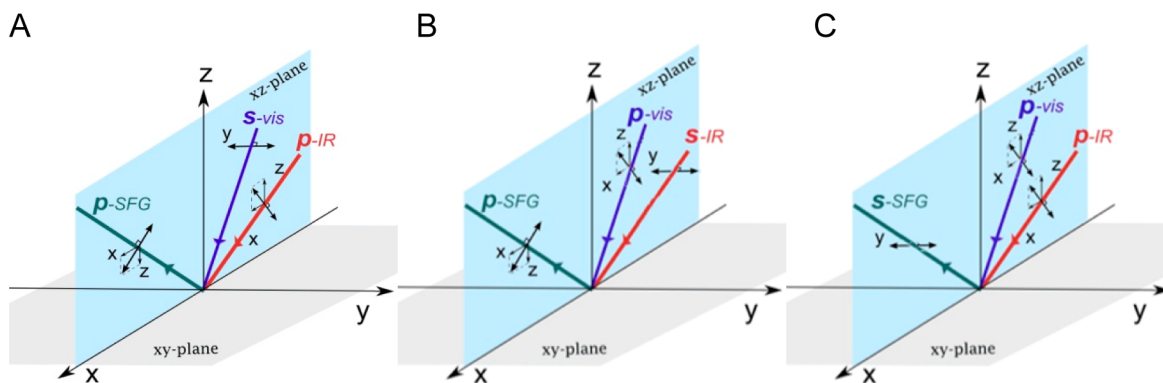
Figure 2. Schematic representation of polarization settings for chiral SFG experiments: the projection of the electric field of *p*-polarized and *s*-polarized light onto the laboratory coordinates.[45] Reprinted with permission. Copyright 2011 MDPI, Switzerland.

$$E_{SFG}^{I} \propto \sum_{JK} \chi_{IJK}^{(2)} E_{VIS}^{J} E_{IR}^{K} \tag{1}$$

where I, J, K (= $x, y,$ or z, the laboratory coordinates) specify the direction of the Cartesian component of the optical fields and $\chi_{IJK}^{(2)}$ is an element of the second-order susceptibility tensor, $\chi^{(2)}$, which contains structural and chemical information about the target medium. Under the electric-dipole approximation, $\chi^{(2)}$ is nonzero only when the medium lacks centrosymmetry. This can be the case for molecular crystals with non-centrosymmetric space groups and the case for buried interfaces. Because molecules at buried interfaces align due to asymmetric physical and chemical forces across two media, the centrosymmetry is broken at interface. In this case, the second-order susceptibility of an interface consists of a nonresonant term, $\chi_{NR}^{(2)}$, and a sum of vibrationally resonant terms, $\chi_q^{(2)}$,[20]

$$\chi^{(2)} = \chi_{NR}^{(2)} + \sum_q \chi_q^{(2)} = \chi_{NR}^{(2)} + \sum_q \frac{A_q}{\omega_{IR} - \omega_q + i\Gamma_q} \tag{2}$$

where A_q is the amplitude, Γ_q is the damping coefficient, ω_q is the resonant frequency of the qth vibrational mode, and ω_{IR} is the frequency of the incident IR beam. The SFG signal is enhanced when ω_{IR} is in resonance with ω_q. Thus, SFG is a surface-specific vibrational spectroscopy.

2.2. Effective Susceptibility of Chiral Surfaces

As presented by Simpson and co-workers,[23,44] the chiral SFG theory will be discussed here by considering the nonzero second-order susceptibility elements of a macroscopic chiral surface and then the relationship of these nonzero susceptibility elements with the experimental observables (i.e., SFG intensity) as well as with the microscopic second-order hyperpolarizability. Such relationships provide a fundamental basis for extracting information about molecular structures and orientations from chiral SFG spectra.

Chiral and achiral surfaces are different in the sense that the former lacks a perpendicular plane of reflection. Thus, a chiral surface adopts C_∞ symmetry, while an achiral surface adopts $C_{\infty V}$ symmetry (Figure 1). For an achiral surface with $C_{\infty V}$ symmetry, there are seven nonzero χ_{IJK} elements: $\chi_{xxz} = \chi_{yyz}$, $\chi_{xzx} = \chi_{yzy}$, $\chi_{zxx} = \chi_{zyy}$, and χ_{zzz}. For a chiral surface with C_∞ symmetry, there are six additional nonzero elements: χ_{xyz}, χ_{yxz}, χ_{zxy}, χ_{zyx}, χ_{xzy}, and χ_{yzx}. These six elements are orthogonal, meaning that $I \neq J \neq K$. Hence, these orthogonal χ_{IJK} ($I \neq J \neq K$) elements are characteristic of chiral surfaces.

The chiral orthogonal χ_{IJK} ($I \neq J \neq K$) elements of an interface can be measured by manipulating the polarization of incident beams and SFG signals. In general, SFG experiments are performed using linearly *s*- or *p*-polarized IR and visible beams while detecting *s*- or *p*-polarized SFG signals (Figure 2). Hence, there are eight possibilities for setting up polarization for an SFG experiment: *ssp* (*s*-polarized SFG, *s*-polarized visible beam, and *p*-polarized IR beam), *sps*, *pss*, *ppp*, *sss*, *psp*, *spp*, and *pps*. For a particular polarization setting, the SFG intensity, I_{SFG}, can be described by the effective second-order susceptibility,

$$I_{SFG} \propto |\chi_{eff}^{(2)}|^2 I_{vis} I_{IR} \tag{3}$$

where $\chi_{eff}^{(2)}$ can be expressed as linear combinations of the second-order susceptibility tensor elements, χ_{IJK}. Thus, the nonzero chiral and achiral elements (Figure 1) can contribute to the eight $\chi_{eff}^{(2)}$:[18]

$$\chi_{ssp}^{(2)} = L_{yy}(\omega_{SFG})L_{yy}(\omega_{VIS})L_{zz}(\omega_{IR}) \sin\alpha_{IR}\chi_{yyz}$$

$$\chi_{sps}^{(2)} = L_{yy}(\omega_{SFG})L_{zz}(\omega_{VIS})L_{yy}(\omega_{IR}) \sin\alpha_{VIS}\chi_{yzy}$$

$$\chi_{pss}^{(2)} = L_{zz}(\omega_{SFG})L_{yy}(\omega_{VIS})L_{yy}(\omega_{IR}) \sin\alpha_{SFG}\chi_{zyy}$$

$$\chi_{ppp}^{(2)} = -L_{xx}(\omega_{SFG})L_{xx}(\omega_{VIS})L_{zz}(\omega_{IR})$$
$$\cos\alpha_{SFG} \cos\alpha_{VIS} \sin\alpha_{IR}\chi_{xxz}$$

$$-L_{xx}(\omega_{SFG})L_{zz}(\omega_{VIS})L_{xx}(\omega_{IR}) \cos\alpha_{SFG} \sin\alpha_{VIS} \cos\alpha_{IR}\chi_{xzx}$$

$$+L_{zz}(\omega_{SFG})L_{xx}(\omega_{VIS})L_{xx}(\omega_{IR}) \sin\alpha_{SFG} \cos\alpha_{VIS} \cos\alpha_{IR}\chi_{zxx}$$

$$+L_{zz}(\omega_{SFG})L_{zz}(\omega_{VIS})L_{zz}(\omega_{IR}) \sin\alpha_{SFG} \sin\alpha_{VIS} \sin\alpha_{IR}\chi_{zzz}$$

$$\chi_{sss}^{(2)} = 0 \tag{4}$$

(A) z-x-z transformation

$$\begin{pmatrix} \cos\phi & -\sin\phi & 0 \\ \sin\phi & \cos\phi & 0 \\ 0 & 0 & 1 \end{pmatrix} \cdot \begin{pmatrix} 1 & 0 & 0 \\ 0 & \cos\theta & -\sin\theta \\ 0 & \sin\theta & \cos\theta \end{pmatrix} \cdot \begin{pmatrix} \cos\psi & -\sin\psi & 0 \\ \sin\psi & \cos\psi & 0 \\ 0 & 0 & 1 \end{pmatrix} = \begin{pmatrix} \cos\phi\cos\psi - \sin\phi\cos\theta\sin\psi & -\sin\phi\cos\theta\cos\psi - \cos\phi\sin\psi & \sin\phi\sin\theta \\ \sin\phi\cos\psi + \cos\phi\cos\theta\sin\psi & \cos\phi\cos\theta\cos\psi - \sin\phi\sin\psi & -\cos\phi\sin\theta \\ \sin\theta\sin\psi & \sin\theta\cos\psi & \cos\theta \end{pmatrix}$$

(B) z-y-z transformation

$$\begin{pmatrix} \cos\phi & -\sin\phi & 0 \\ \sin\phi & \cos\phi & 0 \\ 0 & 0 & 1 \end{pmatrix} \cdot \begin{pmatrix} \cos\theta & 0 & \sin\theta \\ 0 & 1 & 0 \\ -\sin\theta & 0 & \cos\theta \end{pmatrix} \cdot \begin{pmatrix} \cos\psi & -\sin\psi & 0 \\ \sin\psi & \cos\psi & 0 \\ 0 & 0 & 1 \end{pmatrix} = \begin{pmatrix} \cos\phi\cos\theta\cos\psi - \sin\phi\sin\psi & -\sin\phi\cos\psi - \cos\phi\cos\theta\sin\psi & \cos\phi\sin\theta \\ \sin\phi\cos\theta\cos\psi + \cos\phi\sin\psi & \cos\phi\cos\psi - \sin\phi\cos\theta\sin\psi & \sin\phi\sin\theta \\ -\sin\theta\cos\psi & \sin\theta\sin\psi & \cos\theta \end{pmatrix}$$

Figure 3. Euler transformations from the molecular coordinates (a, b, c) to laboratory coordinates (x, y, z). (A) The *z-x-z* transformation. (B) The *z-y-z* transformation. The Euler transformation matrices on the right-hand side are yielded by the multiplication of the three rotational matrices on the left-hand side corresponding to the rotational operations.

$$\chi_{psp}^{(2)} = L_{zz}(\omega_{SFG})L_{yy}(\omega_{VIS})L_{xx}(\omega_{IR})\sin\alpha_{SFG}\cos\alpha_{IR}\chi_{zyx}$$
$$- L_{xx}(\omega_{SFG})L_{yy}(\omega_{VIS})L_{zz}(\omega_{IR})\cos\alpha_{SFG}\sin\alpha_{IR}\chi_{xyz}$$

$$\chi_{spp}^{(2)} = L_{yy}(\omega_{SFG})L_{zz}(\omega_{VIS})L_{xx}(\omega_{IR})\sin\alpha_{VIS}\cos\alpha_{IR}\chi_{yzx}$$
$$- L_{yy}(\omega_{SFG})L_{xx}(\omega_{VIS})L_{zz}(\omega_{IR})\cos\alpha_{SFG}\sin\alpha_{VIS}\chi_{yxz}$$

$$\chi_{pps}^{(2)} = L_{zz}(\omega_{SFG})L_{xx}(\omega_{VIS})L_{yy}(\omega_{IR})\sin\alpha_{SFG}\cos\alpha_{VIS}\chi_{zxy}$$
$$- L_{xx}(\omega_{SFG})L_{zz}(\omega_{VIS})L_{yy}(\omega_{IR})\cos\alpha_{SFG}\sin\alpha_{VIS}\chi_{xzy}$$

$$(5)$$

where the α_i is the incident or reflected angle of the ith laser beam and $L(\omega_i)$ is the tensorial Fresnel factor at frequency ω_i.[18] As shown in eqs 4 and 5, among the eight polarization settings, the *psp*, *pps*, and *spp* settings are related to the chiral orthogonal $\chi_{IJK}^{(2)}$ $(I \neq J \neq K)$ susceptibility tensor elements and thus can be used in chiral SFG experiments. The physical pictures relating the chiral effective susceptibility ($\chi_{psp}^{(2)}$, $\chi_{pps}^{(2)}$, and $\chi_{spp}^{(2)}$) and the chiral orthogonal $\chi_{IJK}^{(2)}$ $(I \neq J \neq K)$ susceptibility tensor elements become clear when one considers the projection of the electric field of *p*-polarized and *s*-polarized light onto the laboratory coordinates with the *z*-coordinate defined as surface normal and *x-z* plane defined as the incident plane (Figure 2). For example, for the *psp* polarization setting (Figure 2A), the *p*-polarized SFG and IR electric fields can be projected onto the *x* and *z* directions; thus, the first and third indices of $\chi_{IJK}^{(2)}$ denoting the polarization electric field for SFG and IR light can only be *x* or *z*. The *s*-polarized visible light has an electric field in the *y* direction only; hence, the second index of $\chi_{IJK}^{(2)}$ denoting the visible-light polarization can only be *y*. Consequently, four tensor elements are relevant: χ_{xyx}, χ_{zyz}, χ_{zyx}, and χ_{xyz}. Among these, the first two are zero as shown in Figure 1. The remaining two orthogonal chiral elements, χ_{zyx} and χ_{xyz}, can therefore be measured using the *psp* polarization setting. Analogously, $\chi_{pps}^{(2)}$ can be expressed by χ_{zxy} and χ_{xzy} (Figure 2B) while $\chi_{spp}^{(2)}$ can be expressed by χ_{yzx} and χ_{yxz} (Figure 2C).

The chiral effective second-order susceptibility tensor elements, $\chi_{psp}^{(2)}$, $\chi_{pps}^{(2)}$, and $\chi_{spp}^{(2)}$, in eq 5 can be simplified further if the Raman polarizability is symmetric, which is often the case when there is no electronic resonance. Under such a condition, $\chi_{xyz} = \chi_{xzy}$, $\chi_{zxy} = \chi_{zyx}$, and $\chi_{yzx} = \chi_{zyx}$. Since the C_∞ point group encompasses the C_4 subgroup, imposition of $x \rightarrow -y$ and $y \rightarrow x$ yields $\chi_{xyz} = \chi_{(-y)xz} = -\chi_{yxz} = -\chi_{xyz} = 0$ and $\chi_{yxz} = \chi_{x(-y)z} = -\chi_{xyz} = -\chi_{yxz} = 0$. Thus, according to eq 5, both χ_{psp} and χ_{spp} are functions of χ_{zyx} only. Similarly, $\chi_{zxy} = \chi_{z(-y)x} = -\chi_{zyx}$ and $\chi_{xzy} = \chi_{(-y)zx} = -\chi_{yzx} = -\chi_{zyx}$. Thus, χ_{pps} is also a function of χ_{zyx} only. Therefore, under vibrationally resonant and electronically nonresonant conditions, eq 5 can be approximated as

$$\chi_{psp}^{(2)} = L_{zz}(\omega_{SFG})L_{yy}(\omega_{VIS})L_{xx}(\omega_{IR})\sin\alpha_{SFG}\cos\alpha_{IR}\chi_{zyx}$$

$$\chi_{spp}^{(2)} = L_{yy}(\omega_{SFG})L_{zz}(\omega_{VIS})L_{xx}(\omega_{IR})\sin\alpha_{VIS}\cos\alpha_{IR}\chi_{zyx}$$

$$\chi_{pps}^{(2)} = \begin{bmatrix} -L_{zz}(\omega_{SFG})L_{xx}(\omega_{IR})L_{yy}(\omega_{IR})\sin\alpha_{SFG}\cos\alpha_{VIS} \\ +L_{xx}(\omega_{SFG})L_{zz}(\omega_{VIS})L_{yy}(\omega_{IR})\cos\alpha_{SFG}\sin\alpha_{VIS} \end{bmatrix}\chi_{zyx}$$

$$(6)$$

Therefore, it follows that under the electric-dipole approximation and in the absence of electronic resonance $\chi_{psp}^{(2)}$, $\chi_{spp}^{(2)}$, and $\chi_{pps}^{(2)}$ are equivalent because they are only related to the same chiral orthogonal susceptibility elements χ_{zyx}. Since this chiral orthogonal susceptibility is zero for achiral surfaces and nonzero for chiral surfaces, the *psp*, *spp*, and *pps* polarization settings can be used to probe surface chirality without interference from the background generated from achiral solute and solvent molecules.

2.3. Surface Susceptibility and Molecular Hyperpolarizability

Because second-order susceptibility of a macroscopic interface is an ensemble average of microscopic hyperpolarizability (β), the effective second-order susceptibility (such as $\chi_{psp}^{(2)}$ for chiral SFG and $\chi_{ssp}^{(2)}$ for achiral SFG) correlates to the hyperpolarizability (β) tensor of molecules at interfaces. The microscopic β tensor determines the SFG response of a

molecule. This response is related to the electric polarizability (α_{ij}), which dictates the selectivity of vibrational Raman spectroscopy and the electric dipole moment (μ_k), which in turn determines the selectivity of vibrational infrared spectroscopy

$$\beta_{ijk,q} \propto \frac{\partial \alpha_{ij}}{\partial Q_q} \frac{\partial \mu_k}{\partial Q_q} \tag{7}$$

where Q_q is the qth normal mode coordinate. Equation 7 implies that the SFG-active vibrational modes must be both IR- and Raman-active. For a macromolecule, such as proteins or DNA, the hyperpolarizability can be calculated by summing the contributions of individual subunits over the spatial arrangement in a macromolecular architecture, as discussed and demonstrated in section 7.

The $\chi^{(2)}_{IJK}$ tensor elements can be expressed in terms of the β_{ijk} tensor elements using the Euler transformation:

$$\chi^{(2)}_{IJK,q} = N \sum_{i,j,k} \langle R_{Ii} R_{Jj} R_{Kk} \rangle \beta_{ijk,q} \tag{8}$$

where I, J, K are the laboratory coordinates (x, y, z) and i, j, k are molecular coordinates (a, b, c); N is the number density of the molecular moiety under study; and R_{Ii}, R_{Jj}, and R_{Kk} are elements of the rotational transformation matrix connecting the molecular coordinates to the laboratory coordinates.

It is worthwhile to mention that Euler transformation can be performed by rotating the laboratory and molecular coordinates using various sequences of rotations, e.g., the z-x-z transformation and z-y-z transformation (Figure 3). Roy et al. has recently discussed practical details in applying such transformation in formulating SFG theory.[46] To express susceptibility tensor elements as a linear combination of the hyperpolarizability tensor elements, the transformation converts molecular coordinates to laboratory coordinates. For the z-x-z transformation, this can be achieved by the clockwise rotation of the molecular c axis by ψ, a axis by θ, and c axis by ϕ to overlap with the laboratory coordinates (Figure 3A). Hence, the z-x-z Euler transformation matrix can be obtained by the multiplication of three matrices corresponding to the three sequential rotations (Figure 3A). Alternatively, the z-y-z transformation can be used, which is achieved by the clockwise rotation of the molecular c axis by ψ, b axis by θ, and c axis by ϕ to overlap with the laboratory coordinates (Figure 3B). Similarly, the z-y-z Euler transformation matrix can be obtained by the multiplication of three rotational matrices (Figure 3B).

In the literature in the SFG field, Euler transformation is often described as rotations of the laboratory axes (x, y, z) in the counterclockwise direction in the sequence of ϕ, θ, and ψ, (left to right in Figure 3). Here, we describe the rotation of molecular axes (a, b, c) in clockwise direction in the sequence of ψ, θ, and ϕ, from right to left, which intuitively corresponds to the sequence of the multiplication of matrices (from right to left) to yield the resulting Euler transformation matrix. Hence, Figure 3 demonstrates the derivation of the Euler transformation matrices that can be applied to project the microscopic hyperpolarizability from the molecular coordinates (a, b, c) to the laboratory coordinates (x, y, z) to yield macroscopic second-order susceptibility.

The z-y-z transformation prevails in most discussions of SFG theory.[47−49] However, the z-x-z transformation is also used.[18] Applications of these two transformations can lead to variations in the definitions of θ, ϕ, and ψ and in the expression of $\chi^{(2)}$

elements in terms of $\beta^{(2)}$ elements. Thus, it becomes necessary to specify the Euler transformation to formulate SFG theory. Regardless of which Euler transformation is used, the physical orientation denoted by the combinations of (ϕ, θ, ψ) should remain the same. In the following discussion, the z-y-z transformation (Figure 3B) is used.

The intensity of the chiral SFG signal measured by the psp polarization is related to $\chi^{(2)}_{psp}$ and consequently $\chi^{(2)}_{zyx}$ in the absence of electronic resonance.[18−20,22,39,45] Similarly, the intensity of the achiral SFG signal measured using the ssp polarization is related to $\chi^{(2)}_{ssp}$, and consequently $\chi^{(2)}_{yyz}$, eq 4. The expressions for these macroscopic susceptibility elements ($\chi^{(2)}_{yyz}$ and $\chi^{(2)}_{zyx}$) can be obtained using eq 8 and the z-y-z Euler transformation matrix (Figure 3B). The Euler transformation introduces the molecular orientation (θ, ψ), while the in-plane rotation angle (ϕ) is averaged by the integration over 0 to 2π for an isotropic interface on the x-y plane to yield:[44]

$$\chi^{(2)}_{ssp} \propto \chi^{(2)}_{yyz} = \chi^{(2)}_{xxz} = \frac{1}{2}N \times$$

$$\left\{ \begin{array}{l} - \langle \sin\theta \cos^2\theta \cos^3\psi + \sin\theta \sin^2\psi \cos\psi \rangle (\beta_{aaa}) \\ + \langle \sin\theta \cos^2\theta \sin\psi \cos^2\psi + \sin\theta \sin^3\psi \rangle (\beta_{aab}) \\ - \langle \sin\theta \cos^2\theta \sin^2\psi \cos\psi + \sin\theta \cos^3\psi \rangle (\beta_{bba}) \\ + \langle \sin\theta \cos^2\theta \sin^3\psi + \sin\theta \sin\psi \cos^2\psi \rangle (\beta_{bbb}) \\ + \langle \cos^3\theta \cos^2\psi + \cos\theta \sin^2\psi \rangle (\beta_{aac}) \\ \quad + \langle \cos^3\theta \sin^2\psi + \cos\theta \cos^2\psi \rangle (\beta_{bbc}) \\ - \langle \sin^2\theta \cos\theta \cos^2\psi \rangle (\beta_{aca} + \beta_{caa}) \\ \quad + \langle \sin\theta \cos^2\theta \cos\psi \rangle (\beta_{acc} + \beta_{cac}) \\ - \langle \sin^2\theta \cos\theta \sin^2\psi \rangle (\beta_{bcb} + \beta_{cbb}) \\ \quad - \langle \sin\theta \cos^2\theta \sin\psi \rangle (\beta_{bcc} + \beta_{cbc}) \\ + \langle \sin^2\theta \cos\theta \sin\psi \cos\psi \rangle (\beta_{abc} + \beta_{acb} + \beta_{bac} + \beta_{bca} \\ \quad + \beta_{cab} + \beta_{cba}) \\ - \langle \sin^3\theta \sin\psi \cos^2\psi \rangle (\beta_{aba} + \beta_{baa}) \\ \quad + \langle \sin^3\theta \sin^2\psi \cos\psi \rangle (\beta_{abb} + \beta_{bab}) \\ - \langle \sin^3\theta \cos\psi \rangle (\beta_{cca}) + \langle \sin^3\theta \sin\psi \rangle (\beta_{ccb}) \\ \quad + \langle \sin^2\theta \cos\theta \rangle (\beta_{ccc}) \end{array} \right\} \tag{9}$$

$$\chi^{(2)}_{psp} \propto \chi^{(2)}_{zyx} = -\chi^{(2)}_{zxy} = -\frac{1}{2}N \times$$

$$\left\{ \begin{array}{l} \langle \cos^2\theta \rangle (\beta_{cab} - \beta_{cba}) \\ + \langle \sin^2\theta \sin^2\psi \rangle (\beta_{bca} - \beta_{bac}) \\ + \langle \sin^2\theta \cos^2\psi \rangle (\beta_{abc} - \beta_{acb}) \\ + \langle \sin^2\theta \sin\psi \cos\psi \rangle (\beta_{aac} - \beta_{aca} - \beta_{bbc} \\ \quad + \beta_{bcb}) \\ + \langle \sin\theta \cos\theta \sin\psi \rangle (\beta_{bab} - \beta_{bba} - \beta_{cac} \\ \quad + \beta_{cca}) \\ + \langle \sin\theta \cos\theta \cos\psi \rangle (-\beta_{aab} + \beta_{aba} - \beta_{cbc} \\ \quad + \beta_{ccb}) \end{array} \right\} \tag{10}$$

Equations 9 and 10 can be simplified further by eliminating the zero hyperpolarizability β elements based on the symmetry
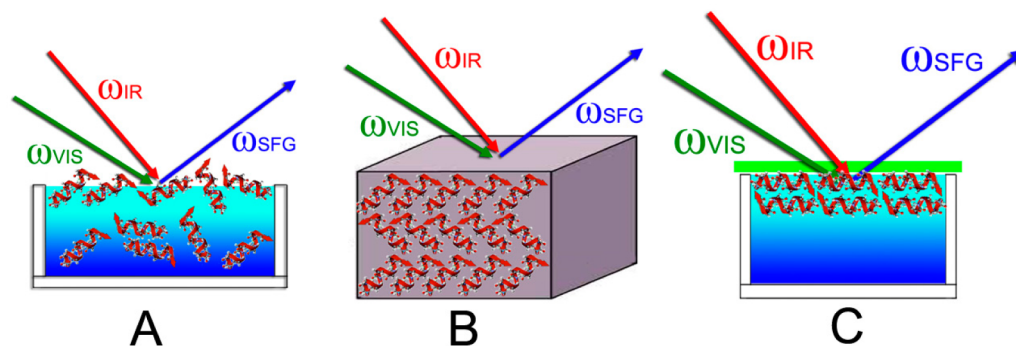
Figure 4. Three cases of interfaces and bulk media with various characteristics of symmetry. (A) An interface of a solution of chiral molecules: the interface has C_∞ symmetry and the bulk is isotropic lacking a reflection plane. (B) A chiral crystal: the interface and the bulk are anisotropic lacking a reflection plane. (C) Two monolayers of chiral molecules oriented in opposite direction at an interface: the two monolayers together are considered as a combined unit with D_∞ symmetry at the interface and the bulk is isotropic.

of macromolecular structures and vibrational modes under study. Hence, a combination of eqs 3, 6, and 10 and eqs 3, 4, and 9 provide quantitative expressions of the experimentally observable I_{SFG} as a function of β_{ijk} and the molecular orientation (θ, ψ) at interfaces for chiral and achiral SFG experiments.

Equation 10 reveals some characteristics of the chiral SFG signals detected from a chiral interface with C_∞ symmetry. First, the chiral SFG signals are contributed not only by the orthogonal chiral β_{ijk} $(i \neq j \neq k)$ elements, but also achiral β elements, suggesting that it is possible for achiral oscillators to contribute to the chiral SFG signals. Second, for chiral macromolecules, the β elements in eq 10 can be calculated by summing the contributions of hyperpolarizability of individual subunits over their spatial arrangements in the chiral macromolecular structures, where the subunits can be amino acids in a chiral protein secondary structure or nucleotides in a DNA molecule, which will be discussed in section 7. Consequently, achiral molecular moieties of the subunits that are in a chiral macromolecular arrangement can contribute to chiral SFG signals, as first proposed by the Simpson group.[23,50] Moreover, the chiral SFG signals originate from the three-dimensional nonlinear susceptibility tensor $\chi^{(2)}_{zyx}$, which is intrinsically capable of reflecting the structural and molecular chirality. On the contrary, conventional chiral-optical methods, such as circular dichroism and Raman optical activity (ROA) rely not only on electric dipole response but also on magnetic dipole and/or electric quadrupole response, which is generally weak. Thus, chiral SFG has relatively high sensitivity in detecting molecular chirality.[5]

2.4. Chiral SFG Response: Bulk versus Interface

Then, does the above theoretical framework suggest that chiral SFG spectroscopy is surface-specific? For a meaningful discussion, we have to attentively specify (1) the experimental conditions and (2) the molecular systems under study; otherwise, there is no definite answer. Here, we confine our discussions under the conditions that the electric-dipole approximation can be applied and electronic resonance is absent. Then, we need to define not only the interface but also the bulk medium for the molecular systems under study using rigorous symmetry terms. Here, we illustrate the importance of such specification using the following three cases (Figure 4A–C).

First, we consider a chiral interface with C_∞ symmetry in contact with a chiral isotropic bulk medium lacking a reflection plane, which can be an interface of a solution of chiral molecules or a pure chiral liquid (Figure 4A). To determine whether chiral SFG is surface-specific, we can compare the quantitative expressions of the chiral SFG signals generated from the surface and from the bulk. The expression for the surface has been derived in section 2.3 starting from C_∞ symmetry (Figure 1), followed by the ensemble average of hyperpolarizability using Euler transformation (Figure 3) to give $\chi^{(2)}_{zyx}$ as in eq 10. Since $\chi^{(2)}_{zyx}$ is directly proportional to the effective chiral susceptibility, $\chi^{(2)}_{psp}$, $\chi^{(2)}_{pps}$, and $\chi^{(2)}_{spp}$, eq 10 provides a quantitative expression of the surface signals. For the bulk chiral signals, the expression has been derived by Shen and co-workers.[51] A chiral bulk medium has isotropic symmetry lacking a reflection plane. Using the symmetry argument similar to the one depicted in Figure 1, one can deduce the following six nonzero second-order susceptibility tensor elements:

$$\chi^{(2)}_{XYZ} = \chi^{(2)}_{YZX} = \chi^{(2)}_{ZXY} = -\chi^{(2)}_{YXZ} = -\chi^{(2)}_{ZYX} = -\chi^{(2)}_{XZY} \propto \chi^{(2)}_{iso}$$

$$(11)$$

where $\chi^{(2)}_{iso}$ is the effective second-order susceptibility, which is a linear combination of the nonzero susceptibility tensor elements. Thus, the effective $\chi^{(2)}_{iso}$ can be calculated as an ensemble average of hyperpolarizability for any one of the six nonzero susceptibility tensor elements in eq 11 by using eq 8. In the calculation, instead of integrating ϕ from 0 to 2π for an isotropic interface, the ensemble average for an isotropic bulk is computed by integrations over three Euler angles: ϕ from 0 to 2π, θ from 0 to π, and ψ from 0 to 2π. The integrations yield the following expression of $\chi^{(2)}_{iso}$, regardless which one of the six nonzero susceptibility elements is calculated or which Euler transformation matrix is used (Figure 3):

$$\chi^{(2)}_{iso} = \frac{N}{6}(\beta_{abc} - \beta_{bac} + \beta_{bca} - \beta_{cba} + \beta_{cab} - \beta_{acb})$$

$$(12)$$

Equation 12 can now be compared with eq 10 to reveal the nature of the bulk and surface chiral SFG signals generated from the molecular system defined in Figure 4A. In the absence of electronic resonance and under the electric-dipole approximation, a Raman polarizability tensor is symmetric.[52] Hence, the first two indices in the hyperpolarizability elements corresponding to the Raman tensor are interchangeable, meaning that $\beta_{abc} = \beta_{bac}$, $\beta_{bca} = \beta_{cba}$, and $\beta_{cab} = \beta_{acb}$. Hence, $\chi^{(2)}_{iso}$ vanishes in eq 12, leading to negligible SFG bulk signals. In fact, in order to observe the SFG signals from the chiral bulk medium, electronic resonance needs to be in place to break the

8476

dx.doi.org/10.1021/cr4006044 | Chem. Rev. 2014, 114, 8471–8498

symmetry of the Raman polarizability tensor, as first reported by Shen and co-workers.[51] On the contrary, according to eq 10, the chiral surface signals do not necessarily cancel, and therefore can be much larger than the vanishing chiral bulk signal in either the reflection or transmittance geometry. Since the chiral SFG signals detected from the bulk is zero in this case, the SFG signals generated from the molecular systems containing a chiral interface with C_∞ symmetry in contact with a chiral isotropic bulk medium lacking a reflection plane (Figure 4A) must come from the chiral interface, leading to the conclusion that chiral SFG is surface-specific.

The second case is a molecular system with a chiral surface and an anisotropic chiral bulk medium, which could be a crystal of chiral molecules or a crystal of achiral molecules with chiral crystal lattice (Figure 4B). Since eq 12 is derived for chiral isotropic bulk, it cannot be applied in this case. In fact, the effective second-order susceptibility of the chiral anisotropic bulk needs to be calculated by an ensemble average of hyperpolarizability using eq 8. In this calculation, the projection from molecular coordinates to the laboratory coordinates depends on the symmetry of the crystal lattice; and the cancellation in eq 12 that is intrinsic to isotropic symmetry cannot be applied to the anisotropic chiral bulk medium for the chiral crystal. On the other hand, for the chiral surface of the crystal, because it is anisotropic lacking inversion symmetry, chiral SFG signals can be in principle generated from the surface. Therefore, chiral SFG spectroscopy is not surface-specific in this case because the signals can be generated not only from the chiral surface but also from the anisotropic chiral bulk medium. In fact, a similar argument can also be applied to conventional (achiral) SFG, where achiral SFG signals can be generated from anisotropic bulk media if the molecules under study are not centrosymmetric.

The third case is an analogy of a lipid bilayer—two monolayers of chiral macromolecules oriented in opposite directions at an interface (Figure 4C). In the research community of nonlinear surface spectroscopy, the rationale of the intrinsic surface-specificity is often conceptually associated with a molecular picture describing the up-versus-down noncentrosymmetry across an interface. This concept is best illustrated by the surface studies of lipid molecules. A monolayer of lipid molecules aligned at an amphiphilic interface has $C_{\infty v}$ symmetry with the breakdown of the up-versus-down inversion symmetry and gives strong SFG signals. A bilayer of lipid molecules has $D_{\infty h}$ symmetry with the up-versus-down inversion symmetry and a reflection plane parallel to the surface. The reflection operation imposes $x \to x$, $y \to y$, and $z \to -z$ such that the nonzero second-order susceptibility elements shown in Figure 1 will vanish, e.g., $\chi_{xzx} = \chi_{x(-z)x} = -\chi_{xzx} = 0$ and $\chi_{zzz} = \chi_{(-z)(-z)(-z)} = -\chi_{zzz} = 0$. Thus, the $D_{\infty h}$ symmetry leads to the cancellation of second-order polarization induced at the upper and lower layers, resulting in no SFG signal.[53−57] An analogy of this lipid bilayer is two monolayers of chiral macromolecules oriented in opposite directions (Figure 4C). The chirality removes the reflection plane and reduces the symmetry from $D_{\infty h}$ to D_∞, which eradicates the achiral susceptibility elements (blue in Figure 1) but preserves the chiral susceptibility elements (red in Figure 1) for a chiral surface. This can be understood by considering the subgroup of C_2 rotation along the x-axis (Figure 1): imposition of $x \to x$, $y \to -y$, and $z \to -z$ to the achiral elements, e.g., $\chi_{xzx} = \chi_{x(-z)x} = -\chi_{xzx} = 0$, lead to cancellation and to the chiral elements, e.g., $\chi_{zyx} = \chi_{(-z)(-y)x} = \chi_{zyx}$, does not lead to cancellation. Thus, the

chiral elements do not cancel even if two monolayers of chiral molecules are oriented in opposite directions at the interface. In this case, chiral SFG may not be considered as surface-specific if the intrinsic surface-specificity of a second-order surface spectroscopy is narrowly defined as the requirement of cancellation in the second-order polarization due to the breakdown of up-versus-down centrosymmetry across an interface.

The above three cases suggest that a meaningful discussion of surface-specificity of chiral SFG spectroscopy requires meticulous specifications of (1) the experimental conditions and (2) symmetry of not only the interface but also the bulk media in the molecular system under study. In short, with the electric-dipole approximation and in the absence of electronic resonance, chiral SFG is surface specific if the interface under study has C_∞ symmetry in contact with an isotropic (chiral or achiral) bulk medium. These conditions are satisfied in numerous important molecular systems, such as proteins in aqueous solution adsorbed on membrane surfaces, DNA and RNA molecules in aqueous solutions detected by biosensors, and functional materials fabricated by the self-assembling process of chiral molecules from the solution onto solid substrates. Therefore, chiral SFG spectroscopy can be applied to study a wide range of important molecular systems to obtain surface-specific information.

In summary, Section 2 provides a theoretical framework for analyzing chiral SFG spectra to obtain information about orientations and structures of chiral macromolecules at interfaces in contact with isotropic bulk media under the electric-dipole approximation and in the absence of electronic resonance. If the hyperpolarizability (β) tensor of the macromolecule is known, the orientation (θ, ψ) can be determined. The β tensor can be obtained either by linear IR[58] and Raman[59] measurements or by computational methods.[47−49,60] The computational methods could be challenging particularly for biomacromolecules owing to their sizes and complexity. Thus, the calculations require various levels of approximation, which will be discussed in Section 7. With respect to structural information, vibrational peaks in the SFG spectra can be assigned to particular vibrational modes of surface structures. This assignment is achieved generally by considering the peak frequencies, selection rules, and symmetries of vibrational modes. This approach can also be aided by quantum-chemistry calculations and normal-mode analyses. Such vibrational analyses and peak assignments can reveal the molecular details of achiral and chiral interfaces.

3. CHIRAL SFG EXPERIMENTS

3.1. Polarization Settings for Chiral SFG Experiments

Specific second-order susceptibility elements can be measured by choosing various polarization settings;[21,23,36,37,41,43] and chiral SFG experiments are often performed using the psp, pps, and spp polarization settings. Equation 5 and Figure 2 shows the relation of the effective $\chi^{(2)}_{psp}$, $\chi^{(2)}_{spp}$ and $\chi^{(2)}_{pps}$ with the nonzero chiral orthogonal χ_{IJK} ($I \neq J \neq K$) elements of a chiral interface with C_∞ symmetry.

Aside from using the three polarization settings (psp, pps, and spp), another polarization setting can also be applied to study surface chirality. This polarization setting is denoted as the pmp polarization, where m denotes the mixed polarization of s and p.[51,61,62] This setting introduces the achiral contribution to interfere with the chiral contribution of the SFG signals. For
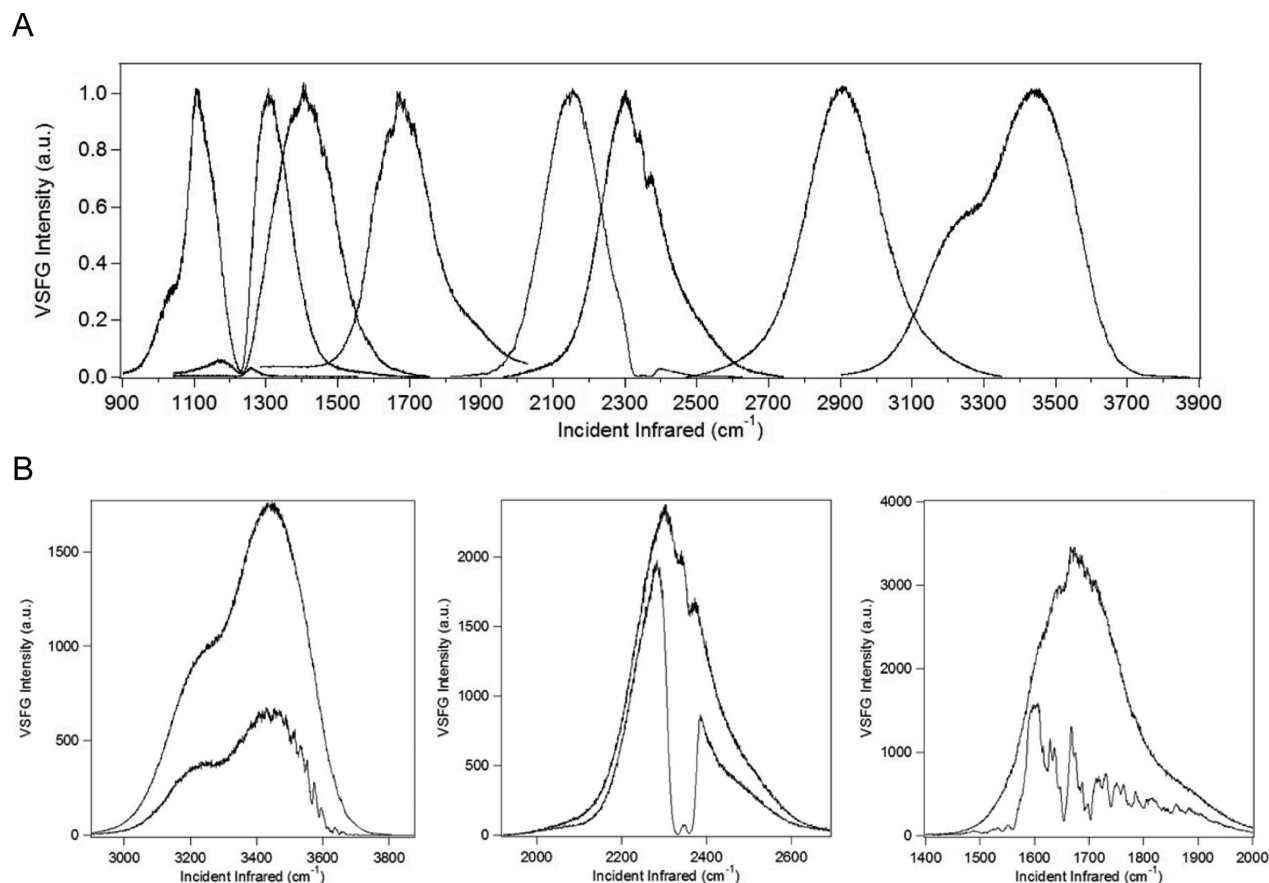
A

B

Figure 5. Characteristics of infrared output of a typical femtosecond broad-bandwidth SFG spectrometer. (A) The IR energy profile indicating bandwidth in the mid-IR 900−3900 cm^{-1} region. (B) Attenuation of IR power due to H_2O and CO_2 in the air: before (bottom curves) and after (top curves) purging of the IR path with dry nitrogen. The O−H stretch of water (left), the O=C=O stretch of carbon dioxide (middle), and the H_2O bending of water (right).[67] Reprinted with permission from ref 67. Copyright 2009 Springer.

example, with the pm+p or pm-p, the effective susceptibility can be expressed as[51,61,62]

$$\chi^{(2)}_{pm\pm p} = \cos(m)\chi^{(2)}_{ppp} \pm \sin(m)\chi^{(2)}_{psp} \tag{13}$$

where m is the polarization angle (usually set to 45° in interference experiments). By subtracting the spectrum taken using the pm-p setting from the spectrum taken using the pm+p setting, the interference terms can be extracted[51]

$$I_{pm+p} - I_{pm-p} = 4\cos(m)\sin(m)\mathrm{Re}(\chi^{(2)}_{ppp}\chi^{(2)}_{psp}) \tag{14}$$

Hence, the interference term includes the chiral effective susceptibility ($\chi^{(2)}_{psp}$), which is related to the chiral orthogonal χ_{IJK} ($I \neq J \neq K$), and thus contains information about surface chirality. As shown in eq 14, if the achiral effective susceptibility ($\chi^{(2)}_{ppp}$) is larger than the chiral susceptibility ($\chi^{(2)}_{psp}$), the chiral term can be increased by the interference effect.

3.2. Spectrometers for Chiral SFG Studies of Biomacromolecules

Two types of SFG spectrometers, scanning spectrometers and broad-bandwidth spectrometers, have been used to perform chiral SFG experiments on biomacromolecules. Scanning spectrometers tune the IR frequency stepwise while measuring the intensity of the reflected signals at each step. Thus, spectral data can be obtained as the frequency is scanned through a vibrational region of interest.[63] The pico- and/or nanosecond laser sources are usually used in scanning spectrometer, which

are less sensitive to the fluctuations in humidity and temperature, and thus maintenance requires relatively less effort. Moreover, the scanning spectrometers often provide relatively high laser power, improving the signal-to-noise ratio. Since the scanning steps can be precisely controlled, scanning systems can generally provide good spectral resolution. In addition, the scanning spectrometers have wide tuning range and vibrational spectra covering 1000−5000 cm^{-1} can be obtained in a single scan without extensive optical alignments. Nonetheless, the frequency scanning makes it cumbersome to set up heterodyne detection that is desirable for providing phase information. Moreover, when the signal-to-noise level is not a limiting factor, the scanning of frequency can limit the time resolution for spectral acquisition for kinetic studies.

Broad-bandwidth spectrometers utilize a femtosecond IR beam and a narrow-bandwidth picosecond visible beam.[64−67] Dictated by the uncertainty principle, a typical 100 fs mid-IR pulse covers a spectral width of 200−300 cm^{-1} (Figure 5). With the broad-bandwidth IR pulses, full spectra of particular vibrational modes, such as C−H stretch at ∼2700−3000 cm^{-1} and amide I region at ∼1600−1700 cm^{-1}, can be acquired shot by shot. Recent developments have also enabled ultrabroadband SFG studies with a spectral width of 600 cm^{-1}.[68] Spectral acquisition shot by shot allows kinetic studies to investigate changes in molecular population, composition, and orientation at interfaces. However, without the use of the pump−probe techniques, the time resolution for kinetic studies is limited by

the signal-to-noise level. Currently, a time scale of minutes has been achieved, which was sufficient to probe kinetics of protein conformational changes in some processes at interfaces.[69−71] Since laser systems have become increasingly powerful and implementation of heterodyne detection methods in SFG experiments can potentially amplify SFG signals,[72−74] the time resolution of kinetic studies using chiral SFG is expected to improve.

For the last two decades, SFG has been extensively applied to study the vibrational modes around ∼3000 cm^{−1}, i.e., ∼3 μm. This can partly be attributed to the fact that ultrafast lasers generally produce high-power IR output in this region, enabling SFG studies of a wide range of molecular systems using a variety of experimental setups. This region covers the stretch frequencies of single bonds, such as the C−H and O−H bonds. Thus, previous studies of biologically relevant molecules using SFG largely focused on the carbon chains of lipid molecules[53,75−77] as well as biomolecules interacting with water molecules.[75,78−80] Recent advancements in laser technology have empowered the SFG method to cover the entire mid-IR regions, making SFG a versatile method for probing the vibrational structures of biological macromolecular structures. For example, the amide I modes of protein backbones at 1600−1700 cm^{−1}, which contain information about protein secondary structures, can now be routinely studied using SFG.[12,45,49,69,70,81−84]

Nonetheless, as the vibrational regions are extended to lower frequencies, attenuation of the IR incident beam along the optical path may occur and precautions need to be taken to avoid that. For example, just as the O−H stretch of water molecules in the air can attenuate the IR power in the ∼3000 cm^{−1} region, the O−H bending of water molecules can attenuate the power in the 1400−2000 cm^{−1} region and the C=O stretch of CO_2 in the 2000−2600 cm^{−1} region (Figure 5). These attenuations can make SFG experiments challenging or even impossible, but they can be overcome by maintaining a low level of humidity in the laser lab (ideally 15−25% relative humidity) and/or enclosing the IR optical path in a compartment purged by dry nitrogen (Figure 5).

In designing SFG spectrometers for studying biological systems, there is a particular concern about photodamage. A desirable SFG spectrometer should not only minimize the pulse energy of the incident beams, but also maintain a signal-to-noise ratio high enough to reveal structural information. Since the repetition rate of pulsed laser is inversely proportional to pulse energy, one strategy is to increase the repetition rate of the pulsed laser source. However, the total laser power of an SFG spectrometer is always a constraint. For a single-amplifier broad bandwidth spectrometer with a fixed total output, the SFG signal is inversely proportional to repetition rate.

$$I_{SFG} \propto \text{repetition rate} \times \frac{\text{IR power}}{\text{repetition rate}} \times \frac{\text{visible power}}{\text{repetition rate}}$$

$$= \frac{\text{IR power} \times \text{visible power}}{\text{repetition rate}}$$

Thus, in designing an SFG spectrometer for probing biological systems, a peculiar setting needs to be identified which minimizes the chance of photodamage in biological samples while maximizing SFG signal to enable a wider range of experiments, such as kinetic and ultrafast pump−probe measurements. Taking the 6-W single-amplifier 100 fs broad bandwidth SFG spectrometer as an example,[67] the repetition

rate is set at 5 kHz. With this setting, the IR power at the sample stage is 20 mW and the pulse energy is at 4 μJ in the C−H stretch region (∼3000 cm^{−1}) while the IR power is 10 mW and the pulse energy is at 2 μJ in the amide I region (∼1600 cm^{−1}).[67] This setting evidently allows acquisition of chiral SFG spectra of proteins without appreciable photodamage at the air/water interface and on solid substrates.

3.3. Surface Platforms for Probing Biomacromolecules

Surface platforms also need to be judiciously considered while designing SFG spectrometers for probing biomacromolecules at interfaces. The choice of the reflection or transmittance geometry should follow the same considerations for conventional (achiral) SFG spectroscopy. Practically, it is determined by the attenuation of the SFG signals and the visible and IR incident beams by the bulk media and is determined also by the optical setups in the SFG spectrometers. Moreover, total internal reflection can also be applied to set up the surface platform to enhance the SFG signal in reflection geometry, as first demonstrated by Richmond and co-workers.[9,10,85] Thus far, only three types of surface platforms have been used for chiral SFG experiments: solid substrates, air/water interface, and solid-supported lipid bilayers. In principle, other surface platforms (Figure 6), such as those used in conventional SFG
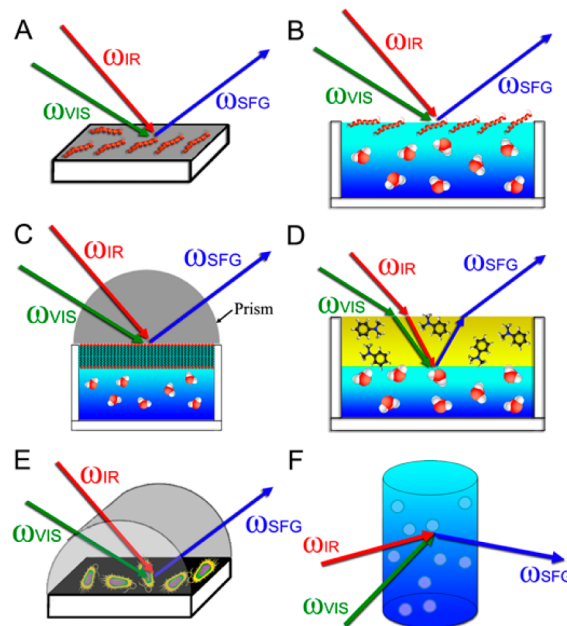
Figure 6. Surface platforms for SFG studies. (A) Solid/air interface, (B) air/water interface, (C) solid supported lipid bilayer, (D) liquid/liquid interface, (E) live cells with temperature and pH controls, and (F) colloidal surfaces in liquid suspension.

experiments, can also be used. These include liquid/liquid, solid/liquid, and liquid/gas interfaces. Moreover, Koelsch and co-workers constructed a setup for SFG studies on live cells.[86] This platform is expected to be useful in addressing a wide range of biomedical problems. In addition, Cremer and co-workers have incorporated microfluidic channels into SFG experiments.[87−89] These channels have the advantages of minimizing sample sizes and streamlining data acquisition under a variety of conditions, potentially allowing SFG experiments to be used in high-throughput experiments. Finally, colloidal surfaces of microparticles and nanoparticles
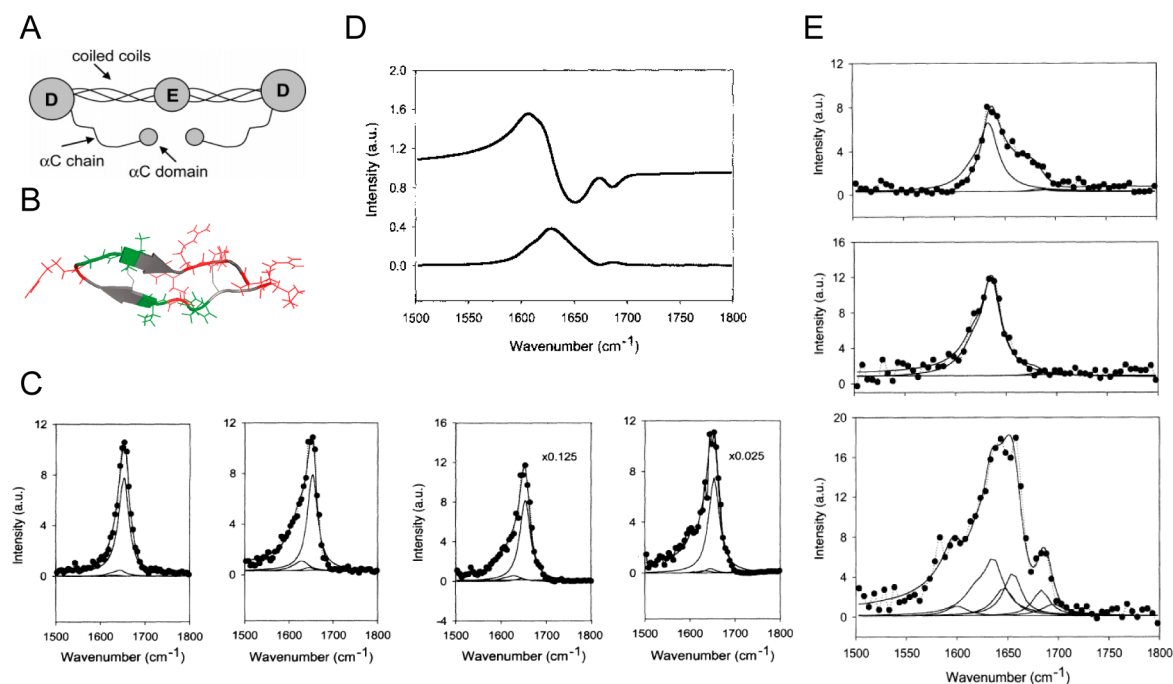
Figure 7. Chiral SFG studies of fibrinogen and tachyplesin I at interfaces. Structures of (A) fibrinogen and (B) tachyplesin I. (C) SFG spectra of fibrinogen layer at polystyrene/water interface: (from left to right) *sp-20°p*, *sp+20°p*, *ssp*, and *ppp*. (D) Deduced chiral (*spp*) SFG vibrational spectra of fibrinogen: (upper) spectrum with a nonresonant background and (lower) spectrum without the nonresonant background. (E) SFG spectra of tachyplesin I at polystyrene/water interface: (upper) *psp*, (middle) *spp*, and (lower) *ssp*. Spectra were obtained with an SFG scanning spectrometer using the visible beam at 532 nm and photomultiplier tube as the detector.[99] Reprinted from ref 99 with permission. Copyright 2005 National Academy of Sciences of the USA.

have been studied using SFG[90] and SHG.[91,92] These colloidal systems include emulsions,[93,94] liposomes,[95,96] metallic nanoparticles,[90,92] and even live bacterial cell suspensions[97] that are highly relevant to biology, biotechnology, and biomedicine. Roke and de Beer considered the theoretical basis for studying vibrational structures of chiral macromolecules of particle suspensions.[98] A challenge for these studies could be that particles in suspension can scatter light; light scattering can potentially alter polarization of the incident beams and SFG signals, jeopardizing the chiral selectivity. Nonetheless, the potential opportunities of using chiral SFG to probe chiral particle surfaces could be particularly exciting because they promise to address important biological problems, such as biomolecular interactions with suspension cell culture and drug delivery across cell membranes.

4. STRUCTURES OF BIOMACROMOLECULES AT INTERFACES PROBED BY CHIRAL SFG

4.1. Chiral Amide I Signals of Proteins or Peptides at Interfaces

While Simpson first proposed the possibility of detecting chiral SFG signals from macroscopic chiral interfaces,[23] Chen and coworkers were the first to experimentally observe the chiral SFG vibrational signals from macromolecular interfacial structures.[99] The Chen group investigated proteins, including fibrinogen[99] and tachyplesin I.[100] Fibrinogen is in a trinodular structure with two outer domains connected by α-helical domains to a central domain (Figure 7A), while tachyplesin I forms antiparallel β-sheets stabilized by a disulfide bond (Figure 7B). The spectra of these two proteins were obtained at the polystyrene/water interface at pH 7.4. By using the interference method, the *sp +20°p* and *sp-20°p* spectra (Figure 7C) were analyzed together

with the *ssp* spectrum to extract the chiral spectra, which exhibit peaks in the amide I region of 1600−1700 cm^{-1} (Figure 7D). These results represent the first observation of chiral SFG response from biomacromolecules at interfaces. Moreover, chiral signals for tachyplesin I at the polystyrene/water interface were directly detected in the amide I region using the *psp* and *spp* polarization settings. The vibrational bands were assigned to the B_1, B_2, and B_3 modes of antiparallel β-sheet structure (Figure 7E), demonstrating the capacity of chiral SFG to characterize protein secondary structures.

Chen's work not only demonstrated the detection of chiral SFG vibrational signals from adsorbed protein in the amide I region at the solid/liquid interface using the interference method but also direct observation of chiral SFG vibrational spectra from an antiparallel β-sheet peptide at the interface. These findings are consistent with the theoretical predictions by Simpson that achiral molecular entities arranged in chiral macromolecular structures can dominate the chiroptical responses of uniaxial systems (C_∞). This work has revealed the potential of chiral SFG as a powerful and unique technique for studying chiral biomacromolecular structures at interfaces and has inspired further experimental developments of chiral SFG for the characterization of chiral biomacromolecular at interfaces.

4.2. Chiral C−H Stretch Signals of DNA on Solid/Water Interfaces

Geiger and co-workers studied the molecular structure of surface-tethered oligonucleotides in both single-strand and duplex forms using vibrational SFG spectroscopy.[62,101] Using 15-mer oligonucleotides, they designed two sequences such that they could elegantly control the structural arrangement of the methyl groups in the thymine (T) nucleotide in the DNA

duplexes. The first sequence was T_{15} with its complementary sequence, A_{15}. The T_{15} single-strand oligonucleotide was covalently linked to a glass surface at the 3′ end, and then the A_{15} complementary oligonucleotide was added to form the $T_{15}{:}A_{15}$ duplex. In this case, the T nucleotides in the DNA duplex were arranged in a helical structure starting from the 3′ end at the interface. The second sequence was T_3A_{12} with its complementary sequence $T_{12}A_3$. The T_3A_{12} single-strand oligonucleotide was covalently linked to the glass surface at the 3′ end, and then the complementary $T_{12}A_3$ oligonucleotide was added to form the $T_3A_{12}{:}T_{12}A_3$ duplex. In this case, the T nucleotides in the duplex were arranged starting from the 5′ end at the interface. Because both strands in a DNA molecule adopt the same handedness in the duplex, the methyl groups in the T-rich strand in both cases have the same physical macroscopic structures, although they are different in directions with respect to the interface (Figure 8A). The *pmp* spectra of both duplexes in the C−H stretch region were obtained using $m = 45°$. Each of the duplexes exhibited differences in the *p+mp* and *p-mp* spectra. For example, Figure 8B shows variations in the *p+mp* and *p-mp* spectra for the $T_{15}{:}A_{15}$ duplex, demonstrating chiral SFG response. A subtraction of the *p-mp* spectrum from the *p+mp* spectrum yielded the difference spectra, which showed opposite signs for the two duplexes. The deoxyribose methane stretch (2900 cm^{-1}) of the DNA backbone was used as a reference and was assigned to be negative. As shown in Figure 8C, the T nucleotide's methyl asymmetric stretch (2960 cm^{-1}) of the $T_3A_{12}{:}T_{12}A_3$ duplex is positive while that of the $T_{15}{:}A_{15}$ duplex is negative. The opposite signs were attributed to the difference in the direction of the T-rich strand in the two duplexes with respect to the interface. As shown in eq 14, the difference between the *p+mp* and the *p-mp* spectra is proportional to the product of $\chi_{ppp}^{(2)}$ and $\chi_{psp}^{(2)}$. With the flip of the T-rich strand by 180°, $\chi_{psp}^{(2)}$ maintains the same, but $\chi_{ppp}^{(2)}$ changes the sign. This leads to the change of the sign for the 2960 cm^{-1} peak corresponding to the asymmetric stretch of methyl groups in the side chains of the T-rich strands. These results illustrate the power of chiral SFG in revealing the directions of chiral arrangements with respect to interfaces in macrobiomolecules.

This work offers a novel approach to probing DNA chirality at interface. It represents the first observation of chiral vibrational signals from DNA duplexes at interfaces due to macroscopic chirality in double helices upon hybridization. It also reaffirms that the macromolecular chiral arrangement can exhibit chiral SFG responses at interfaces,[23,24] which is valid not only in proteins but also in DNA molecules. The observation of the chiral C−H stretch signals from DNA molecules suggests that the chiral SFG studies can be expanded to other chemical groups, such as the N−H, phosphate, and C−N groups. In addition, the observations of sequence-specific hybridization upon formation of the DNA duplexes by chiral SFG also point to further potential applications of chiral SFG in probing biomolecular recognition without introducing external labels, such as fluorescent probes. This capacity suggests that chiral SFG could be useful in addressing a variety of important biological questions at the molecular level, such as molecular recognition in ligand−protein, protein−DNA, and protein−RNA interactions.
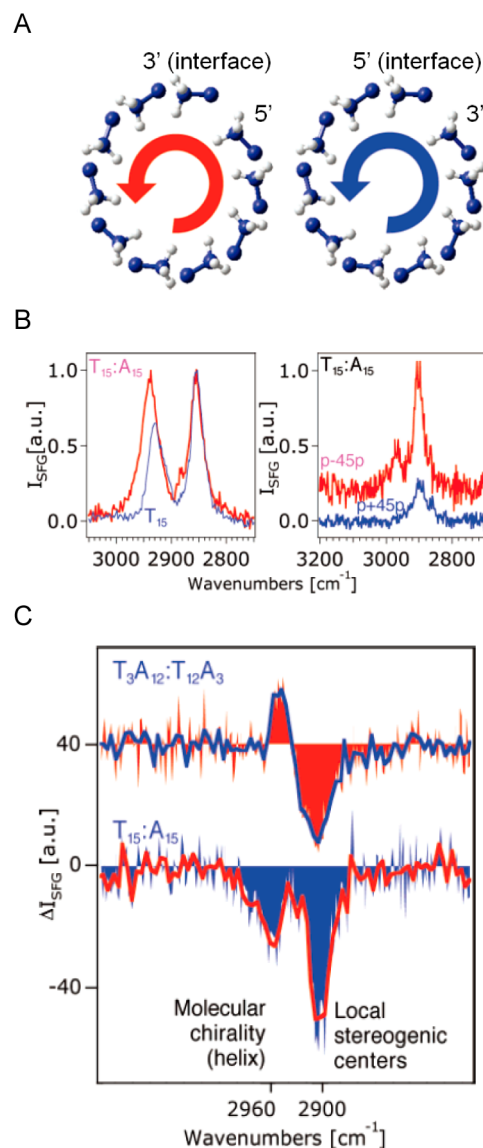
Figure 8. Chiral SFG characterization of 15-mer oligonucleotides in duplex. (A) Top view of a surface-bound oligonucleotides: $T_{15}{:}A_{15}$ (left) and $A_{15}{:}T_{15}$ (right). (B) The *ssp* (left) and *pmp* (right) SFG spectra of the $T_{15}{:}A_{15}$ duplex. (C) The difference spectra of the *p+mp* and *p-mp* spectra of the $T_{15}{:}A_{15}$ and $T_3A_{12}{:}T_{12}A_3$ duplex. The spectra were obtained using broadband SFG spectrometer with femtosecond IR probe pulses and picosecond visible pulses.[62] Reprinted from ref 62 with permission. Copyright 2007 American Chemical Society.

4.3. Chiral N−H Stretch from Protein Backbone at Interfaces

Aside from the amide I band, the N−H stretches of peptide backbones should also contain protein structural information because the N−H groups participate in the H-bonding interactions that stabilize protein secondary structures. However, analysis of N−H stretches using conventional techniques such as Raman scattering and IR absorption are oftentimes difficult due to their overlaps with the O−H stretches of water. Chiral SFG, on the other hand, can detect chiroptical responses from achiral molecular entities arranged in macromolecular chiral architectures. Consequently, the N−H stretch along chiral peptide backbones could be detected in chiral SFG spectra, but the O−H stretch of water, lacking any chiral macroscopic structure, would be silent. Indeed, our group

was able to observe the chiral N–H stretch signals of protein backbone at the air/water interfaces free of water background.[70] For example, Figure 8A shows the chiral SFG spectrum of the peptide of LK$_7\beta$ obtained using the *psp* polarization setting at the air/water interface.[84] The peptide, with a sequence of LKLKLKL, is highly amphiphilic and is known to form antiparallel β-sheet at the air/water interfaces.[102] The peptide was dissolved in phosphate buffer (10 mM, pH 7.4). The formation of antiparallel β-sheet structure is supported by the chiral amide I spectra of LK$_7\beta$ at the air/H$_2$O and air/D$_2$O interface (Figure 9B). The amide I spectra show the
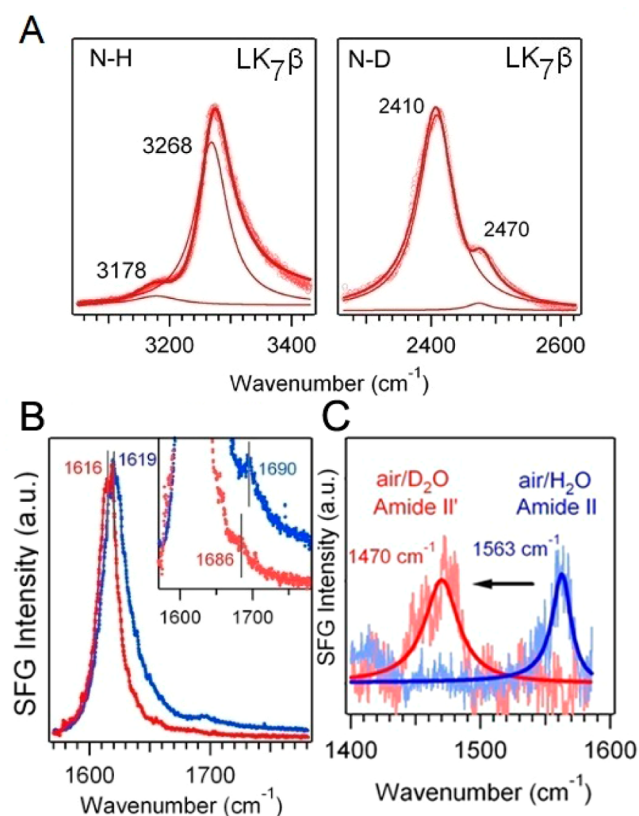

Figure 9. Chiral N–H stretch from protein backbone at interfaces. (A) Experimental chiral SFG spectra of nondeuterated and deuterated antiparallel β-sheets at the air/water interface. (B) Chiral amide I spectra of LK$_7\beta$ at the air/H$_2$O interface (blue) and the air/D$_2$O interface (red). (C) Chiral SFG spectrum of LK$_7\beta$ at the air/water interface in the region of 1300−1600 cm^{-1}.[84] Reprinted from ref 84 with permission. Copyright 2013 American Chemical Society.

characteristic amide I B$_2$ modes at 1619 cm^{-1}, which is shifted slightly to the red upon H/D exchange as expected. The chiral N–H stretch spectrum exhibits a peak at 3268 cm^{-1} and a shoulder at 3178 cm^{-1}, while the chiral N–D stretch spectrum exhibits a peak at ∼2410 cm^{-1} and a shoulder at ∼2470 cm^{-1}.

The observations of the shoulder peaks in Figure 9A demonstrate the capability of chiral SFG in probing subtle vibrational structures in the N–H/N–D stretch region. Since the spectra are free of interference from the background water O–H/O–D stretch, they reveal the shoulder peaks that have remained largely unexplored in previous conventional vibrational studies. The major peaks at 3268 and 2410 cm^{-1} were assigned to the N–H and N–D stretches of the peptide backbone, respectively, in agreement with previous FTIR studies[103] and ab initio calculation.[84] Then, the shoulder peak

at 2473 cm^{-1} in the N–D spectrum was hypothesized to arise from Fermi resonance of a combination band of C–N stretching and N–D in-plane bending with the N–D stretching, as suggested by Mirkin and Krimm.[104] This assignment, however, needs to be verified by the chiral C–N stretch and N–D bending SFG spectra. Nonetheless, the assignment of the shoulder peak at 3178 cm^{-1} in the N–H spectrum is more definitive. The chiral amide II spectrum of LK$_7\beta$ (Figure 9C) was also obtained, showing a peak at 1563 cm^{-1}. The combination band of amide I (1619 cm^{-1}, Figure 9B) and amide II (1563 cm^{-1}, Figure 9C) is at 3182 cm^{-1}, close to the frequency of the shoulder peak at 3178 cm^{-1}. Hence, the 3178 cm^{-1} peak was assigned to the Fermi resonance of the combination mode of amide I and amide II.

These results demonstrate that chiral SFG has the requisite selectivity of chirality and interface to probe the N–H/N–D stretch of peptides free of the O–H stretch water background. Since the peptide N–H groups form H-bonds with the amide carbonyl groups to stabilize various secondary structures and since the N–H stretch frequency is sensitive to the H-bonding environments, the shift in frequency of the N–H stretch can provide information for characterizing protein secondary structures. Moreover, the chiral spectra reveal detailed coupling of various vibrational modes of the peptide backbones in the N–H/N–D regions, including amide I, amide II, C–N stretching, and their various overtones and combination bands. Further characterization of these vibrational modes using chiral SFG is expected to provide useful spectroscopic methods to address fundamental questions in vibrational couplings and vibrational energy distribution in proteins.

4.4. Chiral N–H Stretch and Amide I for Probing Secondary Structures at Interfaces

Since protein secondary structures are constructed by hydrogen bonds between the peptide N–H and amide carbonyl C=O moieties, the N–H stretch frequency also contains information about protein secondary structures. Our group has combined the chiral N–H stretch SFG signals of protein backbones with the chiral amide I signals to establish a set of vibrational signatures to distinguish protein secondary structures at interfaces. There are a number of conventional methods for characterizing protein secondary structures. However, these methods lack either sensitivity to interfaces or selectivity to secondary structures. For example, NMR, EPR, and circular dichroism (CD) do not have surface selectivity, while surface plasmon resonance (SPR) is insensitive to secondary structure. X-ray scattering can probe interfacial ordered structures, but this method is limited in real-time studies. Conventional Raman and infrared (IR) methods are not surface-selective and require metal substrates to enhance surface signal or reflection geometry to suppress bulk signals. These conventional vibrational methods target protein secondary structures by using amide I bands, which overlap with the water bending mode. Thus, D$_2$O needs to be used as solvent. Given that hydrogen bonds are stronger in D$_2$O, this substitution may perturb protein structures and dynamics. Moreover, the amide I signatures overlap for various secondary structures, which makes spectral deconvolution difficult. For example, the use of the amide I frequency for distinguishing α-helices, 3$_{10}$-helices, and disordered structures can be somewhat arbitrary.

Our group obtained the chiral SFG spectra for a series of model peptides and proteins (Figure 10A) at the air/water interface in the amide I region (Figure 10B) as well as the N–H
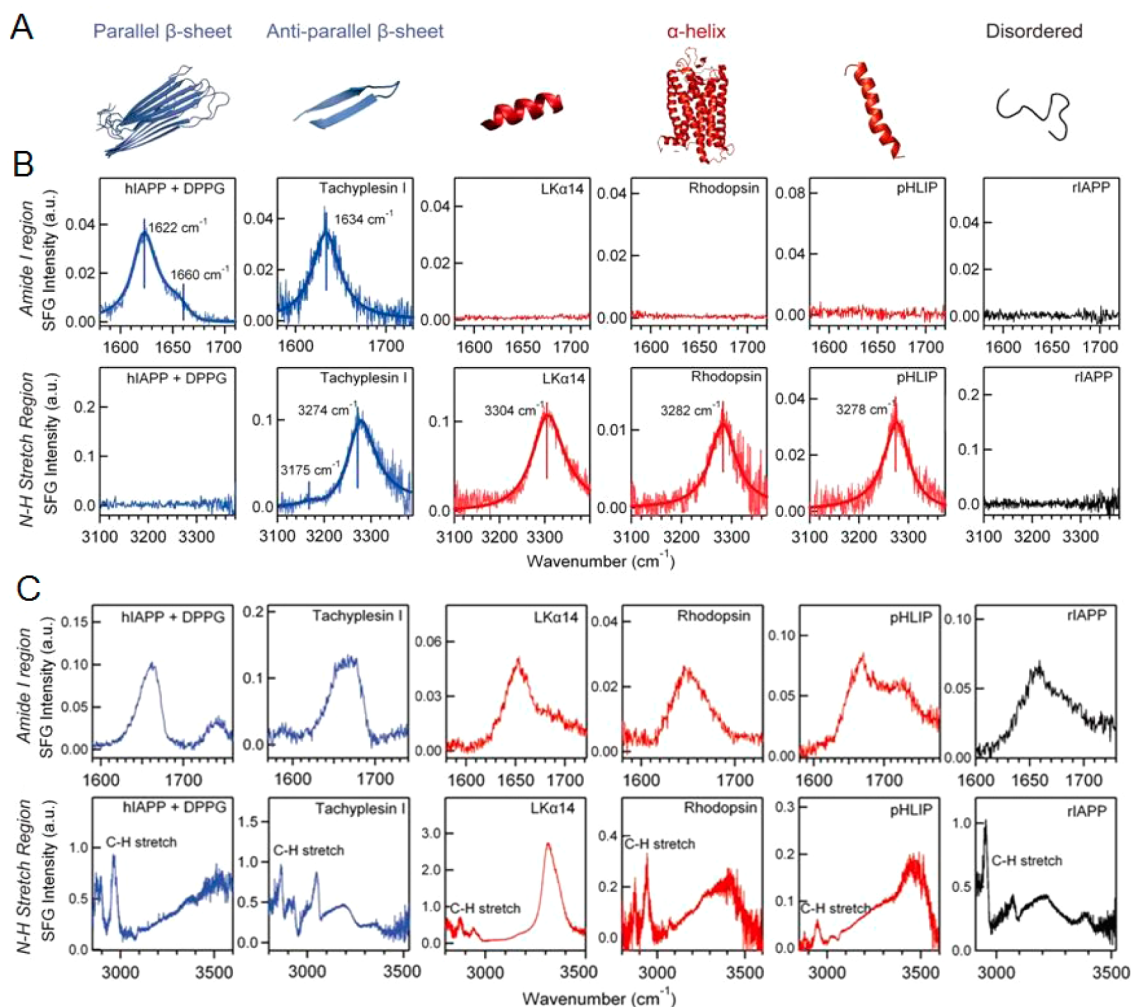
Figure 10. Chiral SFG spectra of model peptides and proteins at interfaces obtained using the *psp* polarization scheme. (A) Schematic diagram of secondary structures for the hIAPP aggregate, tachyplesin I, LK$_\alpha$14, rhodopsin, pHLIP, and rIAPP. (B) The chiral SFG spectra of the model peptides and proteins at the air/water in the amide I region (upper) and the N−H stretch region (lower). (C) Achiral *ssp* SFG spectra of the model peptides and proteins at the air- in the amide I region (upper) and the N−H stretch region (lower).[45] Reprinted with permission from ref 45. Copyright 2011 MDPI, Switzerland.

region (Figure 10B).[45] The model systems include human islet amyloid peptide (hIAPP) aggregates in parallel β-sheets in the presence of lipid molecules, tachyplesin I in antiparallel β-sheets, bovine rhodopsin, pH-low insertion peptide (pHLIP), and LK$_\alpha$14 in α-helical structures. Rat islet amyloid polypeptide (rIAPP) was used as a control system for disordered structures. In the chiral SFG spectra (Figure 10B), parallel β-sheets in hIAPP aggregates exhibit amide I peaks at 1622 and 1660 cm^{-1}. Antiparallel β-sheets of tachyplesin I display chiral N−H at 3274 and 3175 cm^{-1}, as well as chiral amide I signals at 1634 cm^{-1}. The α-helices display N−H signals at 3280 cm^{-1} (rhodopsin and pHLIP) and 3300 cm^{-1} (LK$_\alpha$14), but no amide I signal. The disordered rIAPP is silent in both chiral N−H stretch and amide I spectra. These results support that chiral SFG spectra can provide background-free vibrational signatures for distinguishing protein secondary structures at interfaces.

In contrast to the chiral SFG spectra (Figure 10B), the corresponding achiral SFG spectra (Figure 10C) of the same series of model proteins and peptides show both amide I and N−H stretching achiral signals regardless of secondary structures. The peaks are generally broad, congested, and require spectral deconvolution to extract structural information.

In the amide I region, all secondary structures gave achiral SFG signals with broad spectral features. In the N−H stretch region, the spectral features of the N−H stretch are masked by the background of water O−H stretch, as in conventional vibrational methods. Thus, detailed vibrational structures, such as the combination band of amide I and amide II of LK$_7\beta$ (Figure 9A), cannot be detected.

Chiral SFG is advantageous over conventional methods in probing protein secondary structures at interfaces because the label-free chiral SFG signals of protein backbones are not only surface-selective but also chiral-sensitive. They are also optically clean and free of interference from solvent background and achiral protein structures. A more comprehensive collection of chiral SFG spectra of model proteins and peptides can potentially establish the method as a new approach for distinguishing protein secondary structures at interfaces, similar to the application of CD spectroscopy for the characterization of protein secondary structures in bulk solution. In addition, further theoretical investigation is required to explain the selectivity of chiral SFG for various vibrational modes of protein backbones in various secondary structures. Such experimental and theoretical work will support the develop-

ment of the chiral SFG method that could potentially overcome the lack of noninvasive methods for in situ and real-time identification of protein secondary structures at interfaces, thus enabling kinetic studies of protein folding at interfaces, surface characterizations of biomaterials and biosensors, and ultrafast dynamic studies of vibrational structures of proteins at interfaces.

4.5. Characterization of Various Vibrational Bands of Collagen

Aside from the aforementioned protein secondary structures, type I collagen fibril was also studied by Knoesen and co-workers whereby they used SFG to characterize vibrational structures of type I collagen fibril that give rise to both the chiral and achiral SFG vibrational signals.[105] Collagens form fibrils in a unique chiral architecture different from common α-helical and β-sheet protein secondary structures. In a collagen fibril, three left-handed coiled chains wind around a common axis to form a right-handed triple helix (Figure 11A). This fibril

Figure 11. Characterizations of various chiral vibrational bands in collagen fibrils. (A) Schematic structure of collagen fibrils. (B) An SFG experiment in the transmission mode and collagen fibril in the incident plane. (C) Chiral (*pps* and *spp*) and achiral (*ppp* and *sss*) SFG spectra of collagen fibrils. Spectra were taken using a scanning SFG spectrometer with a visible beam at 532 nm and an IR beam in the range of 1200–3400 cm^{-1}.[105] Reprinted from ref 105 with permission. Copyright 2007 Cell Press.

structure can be constructed on a macroscopic scale, a few hundred of micrometers wide and ~1 cm long. In this study, the SFG characterization is different from the chiral SFG studies discussed earlier in two ways. First, a single collagen fibril (Figure 11B) on a solid substrate was aligned in the incident plane. This can eliminate variability in orientation angles to simplify the spectral analyses. Second, the SFG signals were detected in the transmittance geometry, instead of the reflection geometry. The vibrational structures of the fibrils were characterized in a spectral region of 1200–3400 cm^{-1} using achiral (*ssp*, *ppp*, and *sss*) and chiral (*pps*, *pps*, and *spp*) polarization settings (Figure 11C). The amide I signals are the strongest in the chiral spectra. The chiral amide III band and the methylene stretch, bending, and wagging modes can also be observed. This work has marked the first report of chiral SFG vibrational spectra of collagen fibrils. The extensive studies covering a wide spectral region with a variety of chiral and achiral polarization settings allow assignments of vibrational bands, revealing structural information about the complex fibril molecules.

These vibrational bands are expected to be useful in probing the molecular interactions of collagen fibrils with other bioactive molecules and water. They can also be useful in studying vibrational energy propagation in the fibril structures to reveal mechanical properties of collagen fibrils in connective tissues. Moreover, the study has provided a direct comparison of chiral and achiral SFG spectra of a complex protein structure, which clearly show distinct selection rules for various vibrational bands in the chiral and achiral polarization setting. In addition, unlike the prominent chiral N–H stretch signals of α-helical structures (~3300 cm^{-1}, Figure 10B), the N–H stretch of the collagen fibril is silent (Figure 11C). This silence is likely due to the difference of molecular symmetry between the collagen triple helical and α-helical structures, which results in distinct selectivity in chiral SFG spectra. This postulation needs to be verified by further chiral SFG characterization of a wider range of biomacromolecules with various chiral architectures. Thus, these further studies not only introduce opportunities to study a variety of biological molecular systems, but also provide essential experimental data for further development of chiral SFG theory.

4.6. Double Resonance for Detecting Chiral SFG Signal from Porphyrin J Aggregates

Ishibashi and co-workers applied vibrational SFG spectroscopy to probe the chiral vibrational structures of porphyrin aggregates using resonance in both vibration and electronic transitions.[106] Since porphyrin is involved in important photobiological processes, such as light harvesting in photosynthesis, a better characterization of photochemical properties relating optical to biological activities is fundamental to understanding energy transfer processes in biological systems. In the experiments, tetrakis(4-sulfonatophenyl)porphyrin (TSPP; Figure 12A) was aggregated onto glass substrates as a thin film containing ~100 monolayers. At low pH, the aggregates exhibit a visible absorption band at 490 nm, named the J band. Although the porphyrin is not chiral, chiral macromolecular structures can be induced in the aggregates using chiral reagents. Tartaric acids in the D- and L-enantiomeric forms as well as in the D/L racemic mixture were added as chiral reagents respectively to prepare three batches of thin films. The SFG experiments were conducted in reflection geometry (Figure 12B) using the visible incident
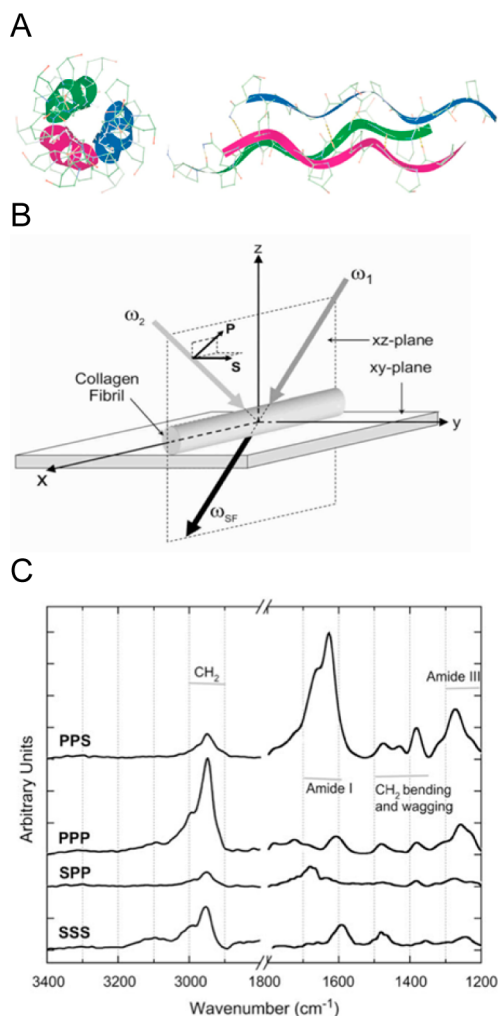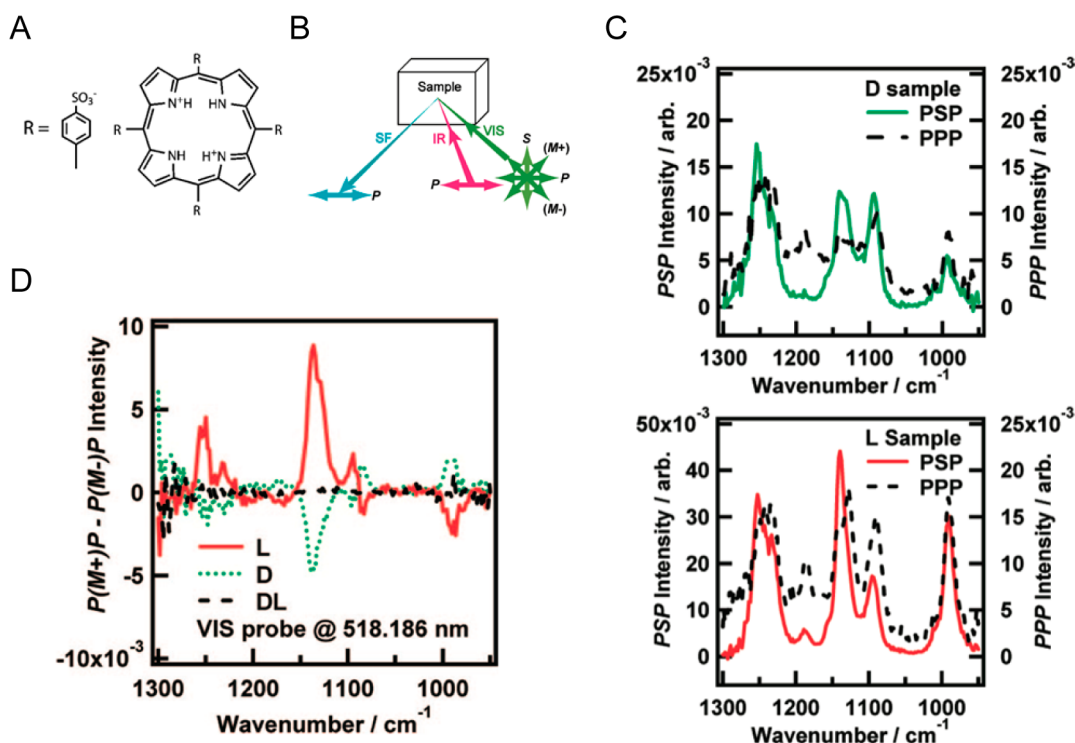
Figure 12. Chiral SFG characterization of J aggregates of porphyrin using double resonance. (A) Tetrakis(4-sulfonatophenyl)porphyrin (TSPP). (B) Reflection geometry and polarization settings of the SFG experiments. (C) SFG spectra of D (upper panel) and L (lower panel) thin film of TSPP aggregates obtained with *ppp* (dashed curves) and *psp* (solid curves) polarization settings. (D) SFG difference spectra between $p(+m)p$ and $p(-m)p$ polarization combinations of thin film samples of TSPP aggregates. The spectra were obtained using broadband SFG spectrometer with femtosecond IR probe pulses and picosecond narrow-band visible pulses at 518 nm.[106] Reprinted from ref 106 with permission. Copyright 2009 American Chemical Society.

beam at 518 nm, preresonant with the J-band transition at 490 nm, and the broad-bandwidth IR beam in the fingerprint region of 950−1300 cm^{-1}. When the D and L forms of tartaric acid were added, the porphyrin aggregates give intense chiral SFG peaks at 990, 1090, 1130, 1190, and 1230−1250 cm^{-1} in the *psp* spectra compared to those of *ppp* (Figure 12C). These fingerprint vibrational bands were assigned to the C−C and C−N stretches and bending vibrational modes in the porphyrin. While the D- and L-porphyrin aggregates exhibit similar *psp*-spectra, their *pmp* spectra show opposite signs for the strongest vibrational band at 1130 cm^{-1} (Figure 12D). This observation agrees with the observations of electronic CD spectra of the D and L forms which show opposite signs. When racemic tartaric acid was used in the preparation of thin films, neither electronic CD nor chiral SFG signals could be observed. These results demonstrate the capability of chiral SFG to elucidate the chirality of thin films of biomolecular aggregates.

This work represents a novel application of double vibrational and electronic resonance in chiral SFG characterization. The additional electronic resonant condition is expected to increase the signal-to-noise ratio for revealing molecular details. Notably, the double resonance conditions could potentially introduce research opportunities to investigate the interplay between transitions with unique chiral selectivity. Such opportunities can potentially unravel the complexity of dynamic processes in light harvesting and internal vibrational energy redistribution in photoactive biological systems. Nonetheless, under electronic resonance conditions, the Raman tensor is no longer symmetric. Thus, the hyperpolarizability tensor not only depends on symmetry of the vibrational modes, as discussed in section 2, but also the

symmetry of the electronic ground and excited states. As a result, calculation of the hyperpolarizability tensors could be challenging, especially for complex biomacromolecular structures. Overcoming this challenge requires further theoretical investigation.

5. ORIENTATIONS OF BIOMACROMOLECULES AT INTERFACES PROBED BY CHIRAL SFG

5.1. Orientation of Antiparallel β-Sheet Structures at Interfaces

Chen and co-workers performed a systematic study on the orientation of antiparallel β-sheets at interfaces.[48] They used chiral SFG in conjunction with conventional (achiral) SFG and attenuated total reflectance Fourier transformation infrared spectroscopy (ATR-FTIR). They studied tachyplesin I, a model peptide that is known to form an antiparallel β-sheet structure stabilized by a disulfide bond. They obtained the amide I spectra using chiral SFG, achiral SFG, and ATR-FTIR with various polarization settings at the polystyrene (PS)/water interface and on the lipid bilayer surface (Figure 13A,B). From these spectra, the tilt angle (θ, the angle between the axis that is parallel to the peptide strand and the surface normal) and twist angle (ψ, the angle rotated about the axis that is parallel to the peptide strand) at interfaces were obtained.

The hyperpolarizability of the antiparallel β-sheet structures was computed for the analysis of the SFG spectra. A bond additivity model was introduced, in which the derivatives of the polarizability and the transition dipole were computed separately by summing up the contributions from individual amino acids spatially arranged in an antiparallel β-sheet
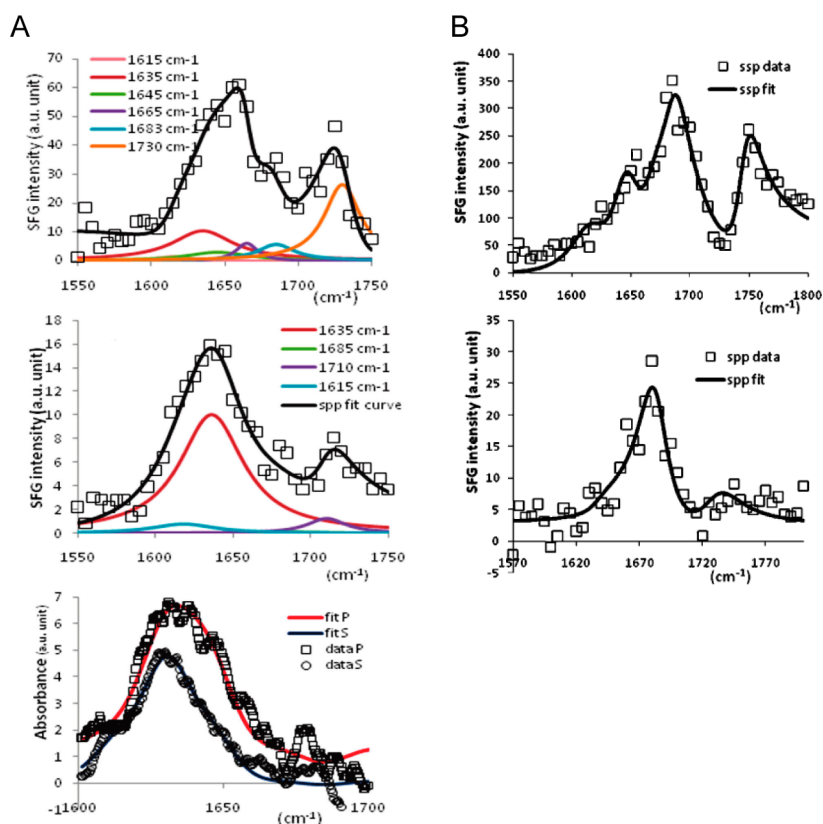
Figure 13. Determination of the orientation of antiparallel β-sheet structures at interfaces with SFG and ATR-FTIR spectra. (A) (upper) Amide I spectrum of tachyplesin I ($\sim$700 nM) adsorbed onto the PS surface in the SFG *ssp* polarization combination, (middle) the SFG *spp* polarization combination, and (lower) the ATR-FTIR amide I band obtained in s and p polarizations. (B) SFG spectrum of tachyplesin I ($\sim$700 nM) adsorbed onto a DPPG/dDPPG lipid bilayer in the *ssp* polarization combination (upper) and the *spp* polarization combination (lower).[48] Reprinted from ref 48 with permission. Copyright 2010 American Chemical Society.

structure. Individual contribution from each amino acid is multiplied by a phase factor to account for the effect of vibrational coupling. Then, the derivatives of the polarizability and transition dipole were multiplied by each other to yield the hyperpolarizability. Since a phase factor is used to describe the effect of vibrational coupling, this approach assumes fully coupled amide I vibrational modes along the peptide backbone.

The calculated hyperpolarizability was then used to analyze the vibrational SFG spectra of tachyplesin I at the PS/water interface. The effective susceptibilities of *ssp* (achiral) and *spp* (chiral) were measured from the SFG spectra (Figure 13A) while analysis of the ATR-FTIR spectra furnished the intensity ratio of the amide I peaks at the s and p polarization settings (Figure 13A). The orientation angles was determined to be $\theta = 76°$ and $\psi = 43°$ for tachyplesin I at the PS/water interface using eq 15:

$$R^{ATR}(\text{amide I}) = \frac{E_x^2}{E_y^2} + \frac{2\langle\cos^2(\theta)\rangle}{3 - \langle\cos^2(\theta)\rangle}\frac{E_z^2}{E_y^2}$$

$$\chi_{ssp}^{(2)} = L_{yyz}\chi_{yyz}^{(2)} = L_{yyz}N_s(\langle\cos^3(\theta)\rangle\langle\cos(\psi)\rangle\langle\sin(\psi)\rangle$$
$$- \langle\cos(\theta)\rangle\langle\cos(\psi)\rangle\langle\sin(\psi)\rangle)\beta_{acb}$$

$$\chi_{spp}^{(2)} = L_{yxz}\chi_{yxz}^{(2)} + L_{yzx}\chi_{yzx}^{(2)} = -\frac{1}{2}L_{yzx}N_s$$
$$(\langle\cos^2(\theta)\rangle - \langle\sin^2(\theta)\rangle\langle\cos^2(\psi)\rangle)\beta_{acb}$$

$$(15)$$

where R^{ATR} is the intensity ratio of the amide I band in the p-polarized to the s-polarized ATR-FTIR spectra; E_x, E_y, and E_z are the components of the electric field vector in the x, y, and z direction; $\chi_{ssp}^{(2)}$ and $\chi_{spp}^{(2)}$ are the effective susceptibilities; L_{yyz}, L_{yxz}, and L_{yzx} are the Fresnel factors; N_s is the surface density of the molecules; and β_{acb} is one of the 27 hyperpolarizability tensor elements. The effective susceptibilities for *ssp* and *spp* were also measured for tachyplesin I at the surface of a lipid bilayer (Figure 13B). In the absence of the ATR-FTIR data, it was noted that θ was within a range of 75–90° and ψ within a range of 75–90°.

This work represents the first systematic approach for quantifying the orientation of the interfacial β-sheet structure in situ using chiral SFG in conjunction with the ATR-FTIR and achiral SFG methods. This work nicely demonstrates the utility of combining theoretical and experimental analyses of SFG spectra to yield molecular information. The bond additivity model for calculating hyperpolarizability is similar to Simpson's approach[47] in considering contributions from individual monomeric units arranged in chiral macroscopic structures, but they differ in their treatment of vibrational coupling, which will be discussed in more details in Section 7. Chen's work has pioneered the use of chiral amide I SFG signals to extract information about orientation of proteins at interfaces

5.2. Orientation of Parallel β-Sheet Structures at Interfaces

In addition to antiparallel β-sheet, parallel β-sheet has also been studied using chiral SFG. Our group, collaborating with the Batista group, applied chiral SFG to measure the orientation of
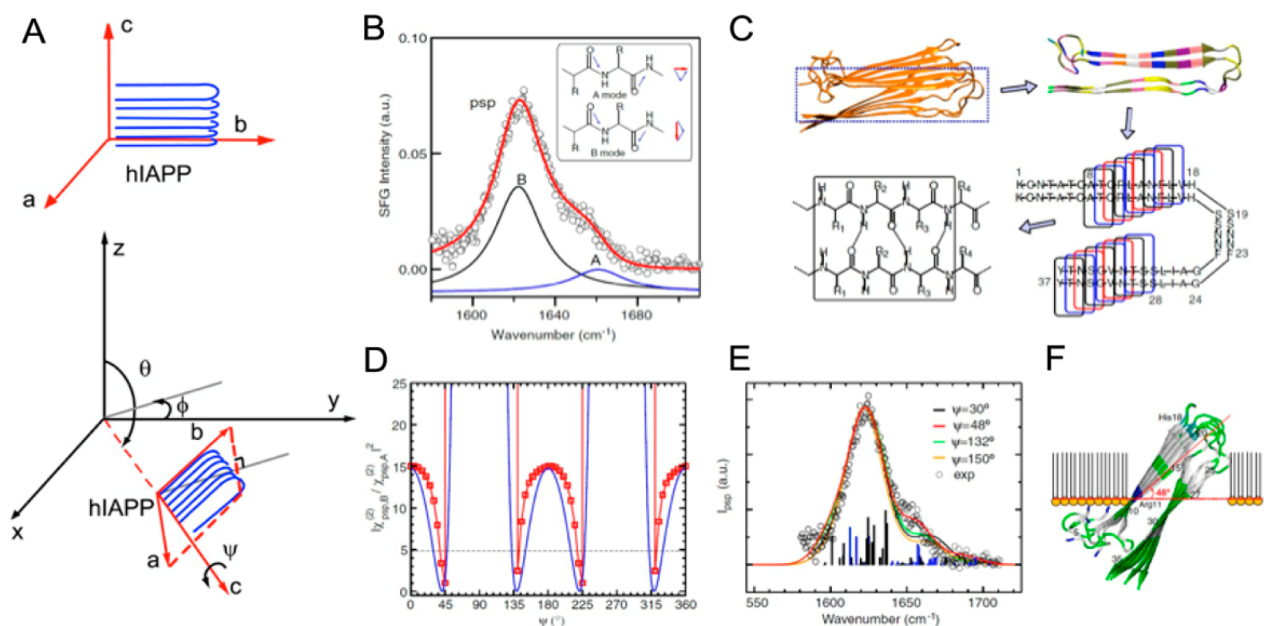
Figure 14. Determination of the orientation of parallel β-sheets formed by hIAPP aggregates at the lipid/water interface. (A) Definitions of the three orientation angles (ϕ,θ,ψ). (B) chiral *psp*-SFG spectrum of hIAPP aggregates, with the blue and black component peaks ascribed to the *A* and *B* amide I modes, respectively. (C) The illustration of the divided-and-conquer method of calculating the hyperpolarizability of the hIAPP aggregates, including dividing the upper and lower β-strand into 18 tripeptide pairs. (D) Square of the ratio of the *B* mode to the *A* mode versus orientation angle ψ, with the blue curve obtained analytically, and the red curve obtained numerically. (E) Simulated chiral SFG spectra of hIAPP aggregates with various orientation at the interface. (F) Representation of Predominant orientation of the hIAPP aggregate at the lipid/aqueous interface.[49] Reprinted from ref 49 with permission. Copyright 2012 Elsevier.

parallel β-sheets formed by human islet amyloid polypeptide (hIAPP) at the air/water interface in the presence of lipid monolayers.[49] The hIAPP peptide with 37 residues has been studied extensively using 2-dimensional IR spectroscopy.[107−109] The peptide aggregates into amyloid β-sheet-rich structures; this aggregation is associated with the onset of type II diabetes. The interactions of β-sheet aggregates with cell membrane are believed to interrupt the integrity of cell membrane, leading to cytotoxicity.[110−112]

Figure 14B shows the chiral *psp* spectrum of hIAPP aggregates in the amide I region, with a major peak at 1620 cm⁻¹ and a shoulder at 1660 cm⁻¹. These peaks are characteristic of parallel β-sheet's amide I antisymmetric *B* and symmetric *A* modes, respectively. Further theoretical analysis shows that the intensity ratio of these two bands depends on the orientation of the parallel β-sheet at the interface:

$$I_{B/A} = \left| \langle \tan^2 \psi \rangle \frac{\beta_{bca,B}}{\beta_{acb,A}} + (1 - \langle \tan^2 \psi \rangle) \frac{\beta_{bac,B}}{\beta_{bac,A}} \right|^2 \quad (16)$$

where ψ is the angle between the β-strands and the interface (Figure 14A). Thus, calculation of the hyperpolarizability elements ($\beta_{acb,A}$, $\beta_{bac,A}$, $\beta_{bca,B}$, $\beta_{bac,B}$) coupled with the measurements of the two peaks' intensity ratio will yield the orientation (ψ). While the intensity ratio is measured to be 4.8 from the fitted amide I spectrum (Figure 14B), the hyperpolarizability was obtained by ab initio quantum chemistry calculation.

Batista and Xiao introduced a divide-and-conquer approach to calculate the hyperpolarizability. The approach first created a molecular model of the parallel β-sheet hIAPP aggregates based on the NMR structure;[113] this model was divided into 16 tripeptide pairs (Figure 14C). The hyperpolarizability of each

tripeptide pair was calculated using ab initio methods and integrated to yield the overall hyperpolarizability of the whole molecular model. With the calculated hyperpolarizability, the relationship between the intensity ratio of the amide I peaks and the orientation of the parallel β-sheet can be plotted (Figure 14D). Although there are several possible orientations (Figure 14D), the chiral SFG spectrum simulated using ψ = 48° shows the best agreement with the experimental data (Figure 14E), suggesting that the hIAPP aggregates orient at the air/water interface with the β-strand at ψ ≈ 48° from the surface (Figure 14F).

This study has established a method for calculating the hyperpolarizability of complex macromolecules and exemplified a general methodology for characterizing the orientation of chiral biomacromolecular structures at interfaces. The approach involves a combination of chiral vibrational SFG spectroscopy and a divide-and-conquer method, using ab initio calculation for simulating SFG spectra. This methodology can be extended to characterize a wide range of systems at interfaces, including but not limited to secondary and tertiary structures of proteins, DNA and RNA molecules, and non-native material, such as peptidomimetics, chiral polymeric, and supramolecular stuctures.

This study has also established an experimental and theoretical framework for probing the early stages of amyloid aggregation at the membrane surfaces. An orientation of 48° of hIAPP β-sheet aggregates at interfaces was found, which could imply a significant disruption of the cell membrane and thus potentially offer insights into pathogenic mechanism of type II diabetes in vivo. More and more studies have shown that lipid membrane catalyzes aggregations of many amyloid proteins[110,114,115] and that the cytotoxicity could arise from the early aggregation intermediates rather than the final aggregation
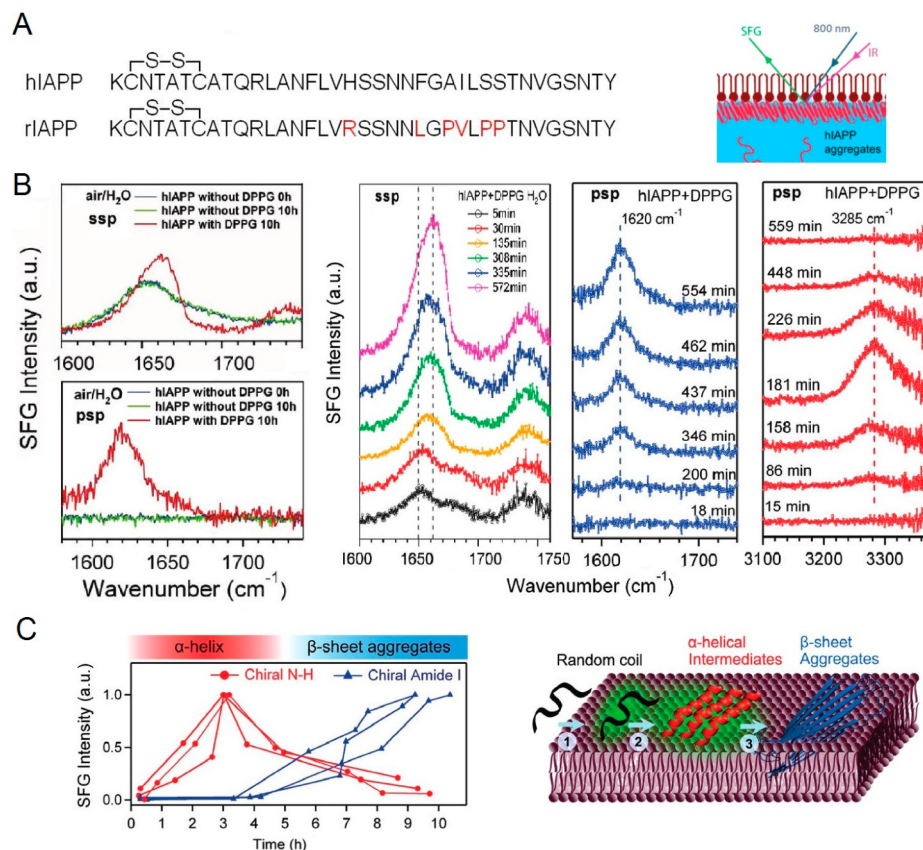
Figure 15. Kinetics of protein folding probed by chiral amide I and N−H stretch. (A) Illustration of hIAPP sequences (left) and the experimental setup (right). (B) Static SFG spectra of hIAPP with interaction with DPPG, with achiral (left upper) and chiral (left lower) polarization setups. The time-dependent SFG spectra of hIAPP with interaction with DPPG at interfaces, with achiral polarization setup in amide I (left), chiral polarization setup in amide I (middle), and chiral polarization setup in N−H stretching regions (right). (C) The intensity of the N−H stretch and amide I signals as a function of time, with triplicate experiments shown and the aggregation model of hIAPP on a membrane surface.[69,70] Reprinted from refs 69 and 70 with permission. Copyright American Chemical Society.

product, fibrils.[116,117] Hence, understanding early stage aggregation on the membrane surface is vital. However, conventional methods cannot distinguish between signals generated from the bulk and those generated from interfaces, thwarting the studies on the interactions between amyloid proteins and membrane surfaces. This work has demonstrated the power of chiral SFG in probing the orientation of the parallel β-sheet amyloid aggregates, introducing an approach for investigating not only the molecular mechanisms of amyloid diseases but also the effects of drug candidates that target the early aggregation intermediates on membrane surfaces.

6. KINETICS AND DYNAMICS OF BIOMACROMOLECULES AT INTERFACES PROBED BY CHIRAL SFG

6.1. Kinetics of Protein Folding Probed by Chiral Amide I and N−H Stretch

Monitoring the kinetics of conformational changes in proteins at interfaces is important for a better understanding of numerous biological phenomena at membrane surfaces, such as the aggregation of amyloid proteins associated with a number of amyloid diseases, such as Parkinson's, Alzheimer's and prion diseases. Aided by the characteristic chiral SFG signatures in amide I and N−H stretching regions as described earlier, our group performed kinetic analyses of protein conformational changes at interfaces using chiral vibrational

SFG spectroscopy.[69,70] The study focused on human islet amyloid polypeptide (hIAPP), a protein associated with type II diabetes.[118,119] This protein is cosecreted with insulin from the islet β-cells of the pancreas and adopts a relatively disordered conformation in the normal state. In the diseased state, however, hIAPP misfolds into amyloid aggregates and deposits in the islet cells of the pancreas; this process is related to the death of the β-cells that produce insulin. Intriguingly, rat islet amyloid polypeptide (rIAPP), which differs from hIAPP by only six amino acids (Figure 15A), does not fold into the β-sheet aggregates and rats do not suffer from type II diabetes. A fundamental understanding of the molecular interactions between hIAPP and lipid membranes, as well as the subsequent misfolding of hIAPP, is necessary to reveal the molecular pathology of type II diabetes at the molecular level.

The static achiral and chiral SFG spectra of hIAPP were obtained at the air/water interface upon interaction with negatively charged lipid 1,2-dihexadecanoyl-*sn*-glycero-3-phospho-(1′-*rac*-glycerol) (DPPG) (Figure 15A). After approximately 10 h, the achiral SFG spectrum exhibits an observable peak shift, while the chiral SFG spectrum exhibits a strong signal at 1620 cm^{-1} with zero water background. Since the 1620 cm^{-1} peak is characteristic of parallel β-sheet structures, the result suggests that the hIAPP forms parallel β-sheets.

Subsequently, three kinetic experiments were performed. First, the time-dependent achiral SFG spectra of hIAPP at the

air/water interface in the amide I regions were obtained upon addition of DPPG lipids. The frequency shift of the amide I peak from 1650 to 1660 cm^{-1} reflects changes in conformation of hIAPP at the interface (Figure 15B). Second, the same experiment was performed using chiral SFG, which clearly showed a gradual signal increase for the 1620 cm^{-1} peak (Figure 15B), suggesting the formation of β-sheets. In the third kinetic experiment, time-dependent chiral SFG spectra of the N–H stretch were obtained; these spectra showed signals at 3285 cm^{-1}. This signal gradually increased, reaching a maximum in 3 h, and then disappeared within 10 h (Figure 15B). The results show that the chiral N–H stretching signal disappears prior to accumulation of the amide I signal (Figure 15C). Because the N–H signal at 3285 cm^{-1} corresponds to α-helical structures, the results indicate a transient α-helical intermediate. These results, combined with the study on hIAPP orientation (section 5.2), led to the following postulation: initially, hIAPP adsorbing onto the membrane surface is relatively unstructured. Upon interaction with the membrane, hIAPP folds into α-helical intermediates. The subsequent conversion of the α-helical intermediates into parallel β-sheet structures results in the insertion of hIAPP into the membrane at a highly tilted angle (~48°) that may facilitate hIAPP's disruption of membrane integrity. Although the correlation between orientation and membrane disruption has yet to be explored, this hypothesis offers new directions in unraveling the pathogenic mechanism for type II diabetes and potentially other amyloid diseases, such as Huntington's, Alzheimer's, and Parkinson's diseases.

This work represents the first kinetic study using chiral SFG to probe conformational changes in biomacromolecules at interfaces in situ and in real time. The kinetic studies were enabled by the use of a broad-bandwidth SFG spectrometer that facilitates shot-by-shot spectral acquisition. The results show that chiral SFG is a method of high selectivity and sensitivity for detecting protein secondary structures. Unlike achiral SFG, the chiral SFG spectra can select for signals associated with the targeted polypeptide, rejecting spectral background from other achiral solute and solvent, such as lipid and water molecules. Based on this result, it is expected that chiral SFG would also be useful for studying the kinetics of conformational changes and molecular interactions of other native and synthetic chiral macromolecular structures at interfaces.

6.2. Kinetics of Proton Exchange in Protein Backbones Probed by Chiral N–H

The kinetics of hydrogen/deuterium (H/D) exchange can provide information about protein structures and dynamics. The H/D exchange has been used as a tool to study interactions of proteins and aqueous solvent, solvent exposure of proteins, and hydrogen-bonding interactions between protein and aqueous environments, revealing molecular details of protein folding,[120] amyloid aggregation,[121,122] and conformational changes of protein upon ligand binding.[123,124] NMR, mass spectroscopy, and Fourier transform infrared spectroscopy have been used to study protein H/D exchange in bulk solution. However, probing H/D exchange in proteins at interfaces is challenging because surface-selective methods are necessary. The observation of protein backbone chiral N–H stretch with zero water background has introduced the opportunity of probing real-time H/D exchange in protein at interfaces.[84]

The experiments were performed using a model system of the amphiphilic LK$_7\beta$ peptide, which forms antiparallel β-sheet structures at the air/water interface (Figure 16A). This peptide
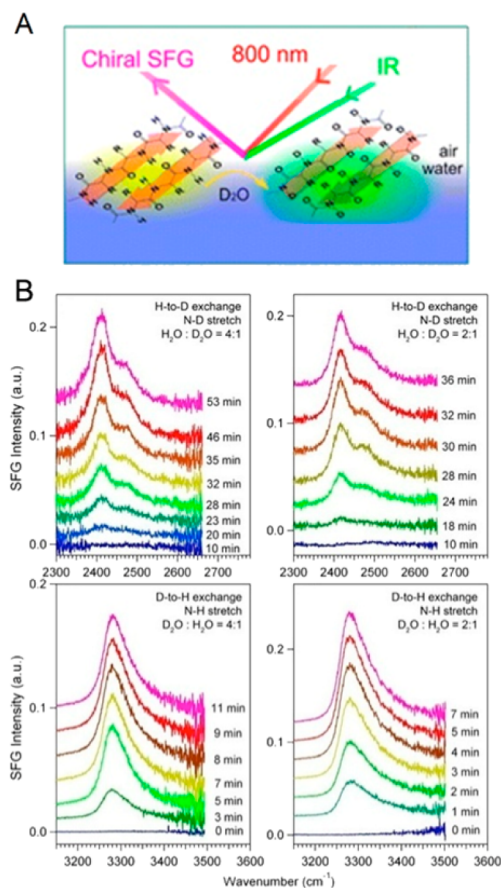

Figure 16. H/D exchange in protein backbones probed by chiral SFG. (A) An antiparallel β-sheet model, with two disulfide bonds formed by cysteine used for chiral SFG experiments and simulations. (B) Kinetics of H/D exchange in LK$_7\beta$ at the air/water interface.[84] Reprinted from ref 84 with permission. Copyright 2013 American Chemical Society.

exhibits chiral SFG spectra in amide I regions at the air/H$_2$O and air/D$_2$O interfaces (section 4.3); these spectra are characteristic of antiparallel β-sheet structures. The N–H and N-D stretch chiral signals of LK$_7\beta$ at the air/H$_2$O and air/D$_2$O interfaces were also observed (Figure 9).

These chiral N–D and N–H stretch signals of LK$_7\beta$ were used to monitor the kinetics of proton exchange in LK$_7\beta$ at interfaces. The H/D exchange process was initiated by addition of D$_2$O into the H$_2$O solution of LK$_7\beta$ or addition of H$_2$O into the D$_2$O solution. Figure 16B shows the time-dependent chiral SFG spectra, which reveal the kinetics of H/D exchange. The N-D signals gradually build up in the case of H-to-D exchange (addition of D$_2$O to H$_2$O) at the final H$_2$O:D$_2$O ratios of 4:1 and 2:1. Similarly, the N–H signals gradually increases in the case of D-to-H exchange (addition of H$_2$O to D$_2$O) at the final H$_2$O:D$_2$O ratios of 1:4 and 1:2. These results demonstrate the ability of chiral SFG for real-time observation of the proton exchange along the peptide backbone of LK$_7\beta$ at the air/water interface. The kinetic results show that the rate of D-to-H exchange is roughly 5–10 times faster than that of H-to-D exchange. Since breaking the O–D or N–D bond requires higher energy than breaking the O–H or N–H bond, the

results suggest that the rate-determining step of the H/D exchange in LK$_7\beta$ at the air/water interface involves breaking the water O−H/O−D bond rather than the peptide N−H/N-D bond.

This work demonstrates a novel application of chiral SFG: probing H/D exchange of proteins at interfaces in situ and in real time. The method relies on the label-free and background-free chiral SFG signals of the N−H/N−D stretch of peptide backbone. This method can potentially be used to study many important biological processes, such as protein folding, protein aggregation, proton transfer in proteins, solvent accessibility of transmembrane proteins, and hydrogen-bonding interactions in transmembrane proteins.

6.3. Kinetics of Protein Self-Assembly Probed by Chiral C−H Stretch of Protein Side Chains

Aside from signals in the N−H stretch and amide I regions, chiral SFG signals in the C−H stretch region have also been used to probe conformational changes in proteins in situ and in real time.[71] The experiments were performed on LK$_7\beta$, which self-assembles into antiparallel β-sheets at the air/water interface using phosphate buffer (pH ~7.4; Figure 17A).[102] Strong chiral SFG signals were observed using the *psp* polarization setting in the C−H stretch region (Figure 17B). When the pH was lowered to ~1.2 with HCl to denature the antiparallel β-sheet structures, the chiral C−H signal vanished (Figure 17B). When the pH was brought back to ~7.4 with NaOH, the chiral C−H signal reappeared (Figure 17B), signifying the self-assembly process. The kinetics of the self-assembly process from the denatured to refolded states was monitored by chiral C−H spectra, with an acquisition time of 1 min (Figure 17C). The intensity of the asymmetric stretch of CH$_3$ at 2958 cm^{-1} was found to increase with time in five independent experiments (Figure 17D). The surface pressure was measured independently during the denaturation and refolding processes (Figure 17E). Altogether, the results indicate that the peptide folds into antiparallel β-sheets in two stages: in the first stage, the peptide adsorbs onto the air/water interface until it reaches a critical population, at which the folding process is initiated; in the second stage, the peptide already at the interface starts folding from disordered forms into more compact β-sheet structures, leaving room for additional peptide molecules in the solution to adsorb at the interfaces. This process continues until the surface population of folded peptide reaches saturation.

The same denaturing and refolding experiments were also monitored by achiral SFG using the *ssp* polarization setting. The results generally show that the achiral SFG spectra of the peptide in the folded and refolded states are not reproducible. Moreover, the time-dependent achiral SFG spectra during the refolding process fluctuate (Figure 17F) instead of exhibiting a trend of a gradual change as in the time-dependent chiral spectra (Figure 17C). These observations suggest that achiral structures of proteins at the interface are largely inhomogeneous. Unlike achiral SFG, chiral SFG is selective to protein chirality, making the chiral SFG method more reliable in probing the kinetics of formation of chiral secondary structures.

This work shows that the C−H stretch detected by chiral SFG can be used as a powerful tool to reveal mechanism of self-assembly process for chiral macromolecular structures in situ and in real time. SFG spectrometers generally provide a higher and more stable IR output in the C−H stretch frequency (~3000 cm^{-1}) than in the lower frequency regions (e.g., amide
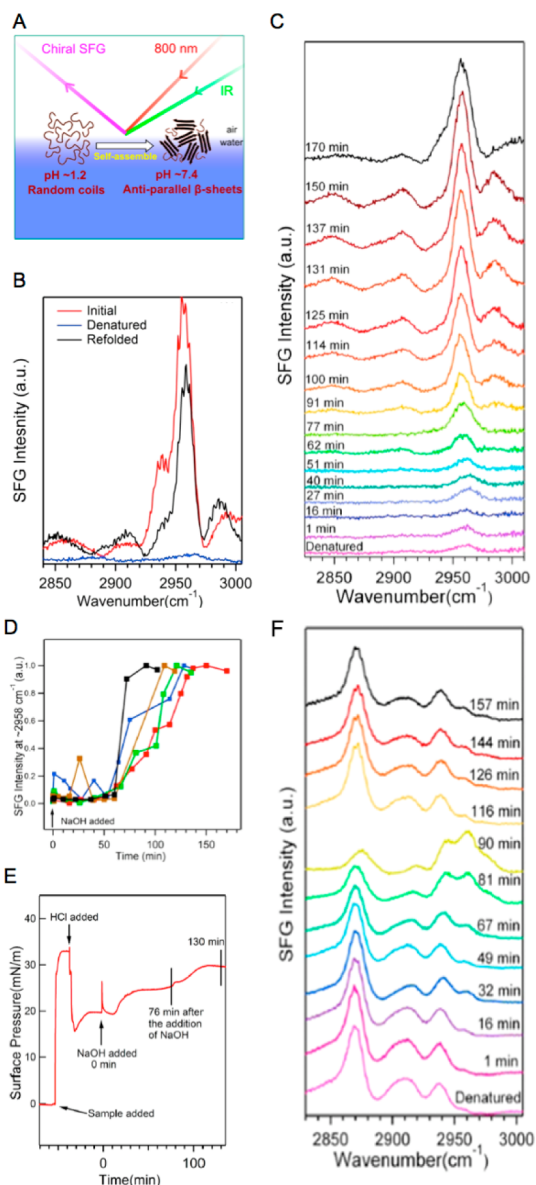
Figure 17. Kinetics of self-assembly of peptides at the air/water interface. (A) Experimental setup and molecular system. (B) Chiral SFG spectra of LK$_7\beta$ at the air/water interface. (C) Time-dependent chiral SFG spectra during the self-assembly of LK$_7\beta$ at the interface. At $t = 0$, NaOH was added. (C) Normalized intensity of the asymmetric stretch of the CH$_3$ peak (2958 cm^{-1}) as a function of time during the self-assembly process in five independent experiments. (D) Changes in surface pressure upon the addition of LK$_7\beta$ (initial adsorption and assembly), HCl (acid denaturation), and NaOH (self-assembly). (F) Time-dependent achiral C−H stretch spectra during the self-assembly of LK$_7\beta$ at the interface.[71] Reprinted from ref 71 with permission. Copyright 2013 American Chemical Society.

I at ~1650 cm^{-1}). Moreover, the IR beam at the C−H stretch frequency is not attenuated by the atmospheric H$_2$O and CO$_2$; consequently, enclosing the IR beam in chambers purged by dry nitrogen gas becomes unnecessary. Consequently, the signal-to-noise level of SFG spectra is generally higher in the C−H stretch region than in the lower frequency regions. Thus, the spectral acquisition times can be shortened and the time resolution of kinetic studies can be improved. Given the abundance of C−H groups, the chiral SFG method is generally applicable to a wide variety of molecular systems that are

important to the fields of biomedical engineering, polymer science, material science, and supramolecular chemistry.[125−127]

7. CALCULATIONS OF HYPERPOLARIZABILITY OF BIOMACROMOLECULES

Chiral SFG spectra provide rich vibrational information about chiral biomacromolecules at interfaces with C_∞ symmetry in contact with isotropic bulk media. As shown in section 2, under the electric-dipole approximation, the susceptibility ($\chi^{(2)}$) tensor elements can be expressed as linear combinations of hyperpolarizability ($\beta^{(2)}$) tensor elements, where the coefficient for each term is a function of Euler angles. Thus, hyperpolarizability values are necessary for the quantitatively interpretation of SFG spectra to yield information about the structures and orientations of biomacromolecules at interfaces. However, calculation of the $\beta^{(2)}$ tensor elements is challenging because large biomolecules generally possess complex macromolecular architectures. Added to this is the sequence specific monomeric units, e.g., amino acids in proteins, the conformations, and the side chains of individual monomeric units can perturb the electronic and vibrational structures of chiral biomacromolecular backbone and may need to be considered in the calculation.[128−131] Due to limitations in computational power, various approximation methods have been used. Thus far, the Simpson,[47] Chen,[48,60] and Batista[49] groups have reported calculations of the hyperpolarizability of protein secondary structures, which are reviewed below.

7.1. Calculation of Hyperpolarizability of Biomacromolecules for Weak Vibrational Coupling

In calculating hyperpolarizability of proteins, Simpson and co-workers treated each amino acid residue as an independent monomeric unit,[47] assuming the coupling between the neighboring residues in a protein secondary structure is negligible. In this case, the hyperpolarizability tensor elements of the monomeric unit can be computed individually and then summed up with a consideration for the spatial arrangement of individual units in the macroscopic protein secondary structure. The summation yields the hyperpolarizability of the overall secondary structures:

$$\beta_{ijk,n}^{1°} \propto \frac{\partial \alpha_{ij,n}^{1°}}{\partial Q_q} \frac{\partial \mu_{k,n}^{1°}}{\partial Q_q} \tag{17}$$

$$\beta_{ijk}^{2°} = \sum_{n=1}^{N_1} \beta_{ijk,n}^{1°} \tag{18}$$

where $\partial \alpha_{ij,n}^{1°}/\partial Q_q$ and $\partial \mu_{k,n}^{1°}/\partial Q_q$ are the derivatives of the Raman polarizability and transition dipole with respect to coordinates of the qth vibrational mode; $\beta_{ijk,n}^{1°}$ is the hyperpolarizability element for the nth amino acid residue and $\beta_{ijk}^{2°}$ is the hyperpolarizability element for the secondary structure; the superscript 1° denotes the amino acid monomeric unit and the superscript 2° denotes the macroscopic the protein secondary structures; and N_1 is the number of amino acids in the model for a secondary structure.

Using the molecular coordinates presented in Figure 18A, Simpson and co-workers computed the hyperpolarizability tensors for α-helix, 3_{10}-helix, parallel β-sheet, and antiparallel β-sheet structures in the amide A (N−H stretch) region and amide I region. They used N-methylacetamide as a model for the monomeric building block of the protein secondary
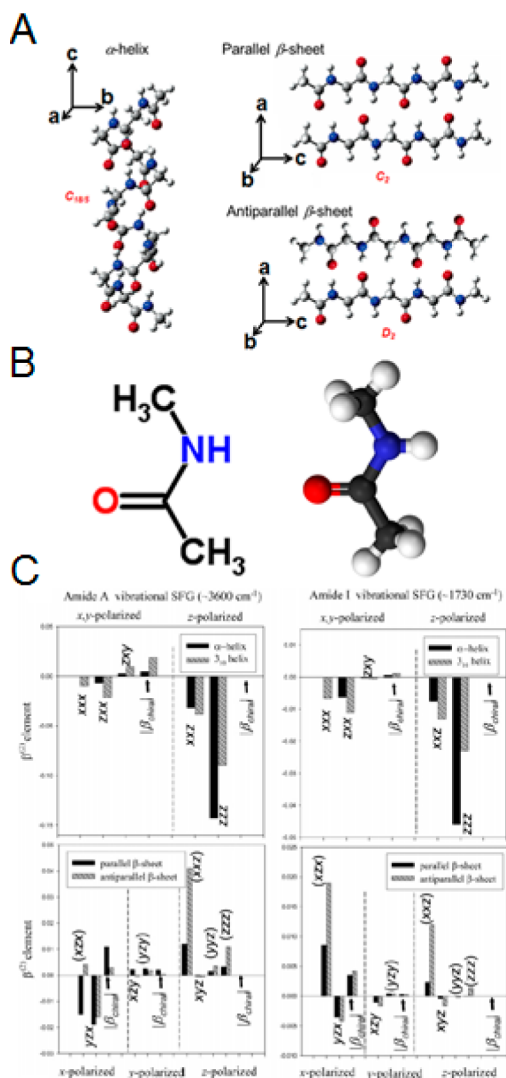

Figure 18. (A) Molecular coordinates for the secondary structures used in the computation. (B) Structure of N-methylacetamide (C) The calculated values of the hyperpolarizability elements for the amide A and amide I vibrational SFG modes for α-helix, 3_{10}-helix, parallel β-sheet and antiparallel β-sheet.[47] Reprinted from ref 47 with permission. Copyright 2005 American Chemical Society.

structures (Figure 18B) and performed ab initio calculation to obtain the hyperpolarizability ($\beta_{ijk}^{1°}$). Since each secondary structure has characteristic symmetry and belongs to a particular point group, some of the tensor elements can be eliminated using group theory. The hyperpolarizability tensor of a secondary structure can be further simplified by considering the symmetry of Raman polarizability tensors. In the absence of electronic resonance, the Raman polarizability tensor is symmetric. Hence, the first two indices in the hyperpolarizability elements that corresponds to the Raman polarizability tensor are interchangeable, leading to 11 nonzero elements for α-helix ($\beta_{ccc}^{2°}$, $\beta_{caa}^{2°} = \beta_{cbb}^{2°} = \beta_{aca}^{2°} = \beta_{bcb}^{2°}$, $\beta_{aac}^{2°} = \beta_{bbc}^{2°}$, $\beta_{acb}^{2°} = -\beta_{bca}^{2°} = \beta_{cab}^{2°} = -\beta_{cba}^{2°}$), six for antiparallel β-sheets ($\beta_{cab}^{2°} = \beta_{acb}^{2°}$, $\beta_{cba}^{2°} = \beta_{bca}^{2°}$, $\beta_{abc}^{2°} = \beta_{bac}^{2°}$), and 13 for parallel β-sheets ($\beta_{ccc}^{2°}$, $\beta_{aac}^{2°}$, $\beta_{bbc}^{2°}$, $\beta_{caa}^{2°} = \beta_{aca}^{2°}$, $\beta_{cbb}^{2°} = \beta_{bcb}^{2°}$, $\beta_{cab}^{2°} = \beta_{acb}^{2°}$, $\beta_{cba}^{2°} = \beta_{bca}^{2°}$, $\beta_{abc}^{2°} = \beta_{bac}^{2°}$). The calculated values of these nonzero $\beta^{(2)}$ elements (Figure 18C) can be used to analyze experimental SFG spectra to obtain structural and orientation information.
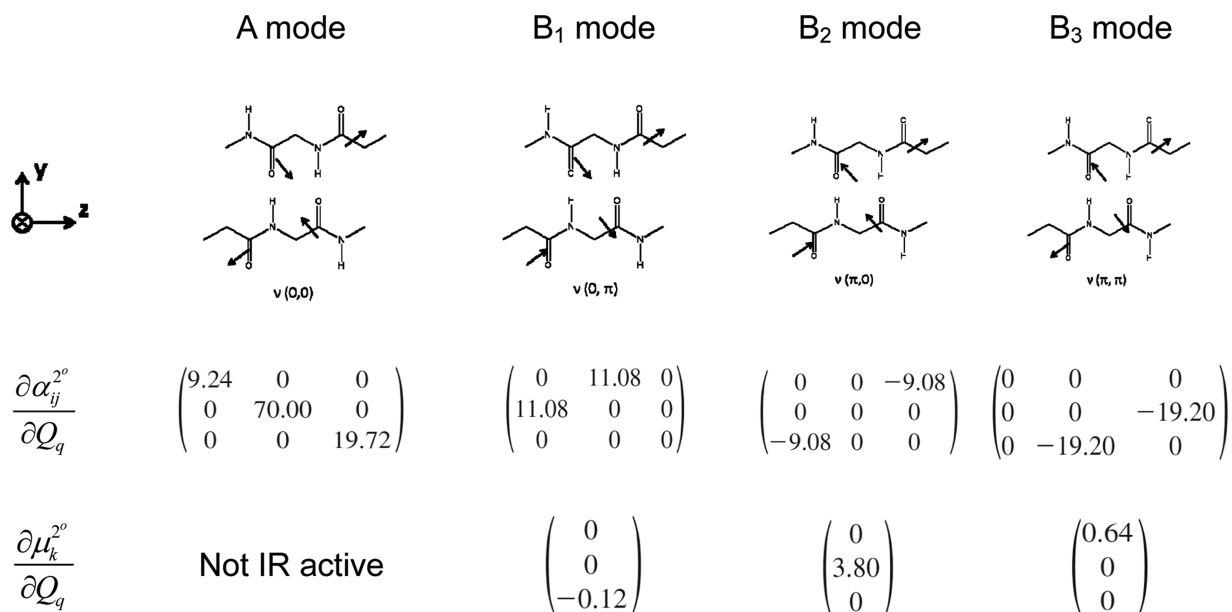
	A mode	B$_1$ mode	B$_2$ mode	B$_3$ mode

$$\frac{\partial \alpha_{ij}^{2^o}}{\partial Q_q} \qquad \begin{pmatrix} 9.24 & 0 & 0 \\ 0 & 70.00 & 0 \\ 0 & 0 & 19.72 \end{pmatrix} \quad \begin{pmatrix} 0 & 11.08 & 0 \\ 11.08 & 0 & 0 \\ 0 & 0 & 0 \end{pmatrix} \quad \begin{pmatrix} 0 & 0 & -9.08 \\ 0 & 0 & 0 \\ -9.08 & 0 & 0 \end{pmatrix} \quad \begin{pmatrix} 0 & 0 & 0 \\ 0 & 0 & -19.20 \\ 0 & -19.20 & 0 \end{pmatrix}$$

$$\frac{\partial \mu_k^{2^o}}{\partial Q_q} \qquad \text{Not IR active} \qquad \begin{pmatrix} 0 \\ 0 \\ -0.12 \end{pmatrix} \qquad \begin{pmatrix} 0 \\ 3.80 \\ 0 \end{pmatrix} \qquad \begin{pmatrix} 0.64 \\ 0 \\ 0 \end{pmatrix}$$

Figure 19. Derivatives of the Raman polarizability and the IR transition dipole in the amide I region for antiparallel β-sheets.[48] Reprinted from ref 48 with permission. Copyright 2010 American Chemical Society.

This work provided a theoretical framework for calculating hyperpolarizability tensors of complex macromolecules through summing the individual contributions of monomeric units within the macromolecular structures. This idea laid a foundation for additional methods that seek to compute hyperpolarizability tensors for complex and large protein secondary structures, aiding further analyses of experimental chiral and achiral SFG spectra of proteins at interfaces.[49] Presumably, this approach can also be extended to other biomacromolecules and biopolymers, including DNA and RNA.

7.2. Calculation of Hyperpolarizability of Biomacromolecules for Strong Vibrational Coupling

According to Chen and co-workers when vibrational interactions between neighboring residues in polypepetides are strong, each residue in the secondary structure can no longer be treated as an independent subunit.[48,60] In this case, derivatives of the Raman polarizability and the transition dipole for a secondary structure should be computed separately with the coherent summation of elements for individual residues adjusted by phase factors. Then, as shown in eqs 19−21, the resulting derivatives of Raman polarizability and transition dipole can be used to compute the hyperpolarizability elements for the secondary structure.

$$\frac{\partial \alpha_{ij,n}^{2^o}}{\partial Q_q} = \sum_{n=1}^{N_1} \frac{\partial \alpha_{ij,n}^{1^o}}{\partial Q_q} e^{i\varphi_n} \tag{19}$$

$$\frac{\partial \mu_{k,n}^{2^o}}{\partial Q_q} = \sum_{n=1}^{N_1} \frac{\partial \mu_{k,n}^{1^o}}{\partial Q_q} e^{i\varphi_n} \tag{20}$$

$$\beta_{ijk}^{2^o} \propto \frac{\partial \alpha_{ij,n}^{2^o}}{\partial Q_q} \frac{\partial \mu_{k,n}^{2^o}}{\partial Q_q} \tag{21}$$

where $((\partial \alpha_{ij,n}^{1^o})/(\partial Q_q))$ and $((\partial \alpha_{k,n}^{1^o})/(\partial Q_q))$ are the Raman polarizability derivative and the transition dipole derivative,

respectively, considered in terms of the coordinate of the qth vibrational mode for the nth residue in the secondary structure; $\beta_{ijk}^{2^o}$ is a hyperpolarizability tensor element for the secondary structure; N_1 is the number of residues in the secondary structure; and $e^{i\varphi_n}$ is the phase factor describing the coupling of vibrating groups in the neighboring residues. Different combinations of the phase angles, φ_n, can be used to describe vibrational coupling between neighboring residues. For example, $(\varphi_1 = 0$ and $\varphi_2 = 0)$ indicate in-phase vibration while $(\varphi_1 = 0$ and $\varphi_1 = \pi)$ indicate out-of-phase vibration in parallel β-sheets.

To determine the hyperpolarizability of secondary structures, Chen and co-workers used the derivatives of the Raman polarizability and the IR transition dipole of monomeric unit obtained in previous Raman[59] and IR[132] studies. These derivatives were then transformed into their molecular frame to yield the hyperpolarizability of the amide I vibration for antiparallel β-sheets. The results were used to analyze the chiral SFG spectra of tachyplesin I to obtain its orientation on polymer surfaces as well as on supported lipid bilayer surfaces (Figure 19).

Chen's work represents the first example of a combined theoretical and experimental chiral SFG spectral study to describe the molecular orientation of biomacromolecules at interfaces; their results suggest that chiral SFG can be used to collect molecular information that is otherwise difficult to obtain.

7.3. Calculation of Hyperpolarizability by the ab Initio Quantum Chemistry Method

Batista and Xiao developed a "divide-and-conquer" method to compute the hyperpolarizability of hIAPP that forms parallel β-sheets at the air/water interface in the presence of lipid monolayer.[49] To compute the hyperpolarizability of the parallel β-sheet structure formed by hIAPP for the amide I vibrational mode, they first divided the β-sheet portion of the peptide NMR structure into 16 tripeptide pairs including the amino acid residues (see Figure 14C in section 5.2). Then, they performed normal-mode analysis using ab initio calculations

and obtained the derivatives of the IR transition dipole and the Raman polarizability for the vibrational modes, contributing to the amide I peaks. Based on the angle (ξ) between the transition dipoles and the backbone of the β-strands, 89 relevant vibrational modes were categorized into either amide I A ($0° \leq \xi < 75°$) or amide I B ($75° \leq \xi \leq 90°$) modes (Figure 20A), taking into consideration the vibrational coupling of

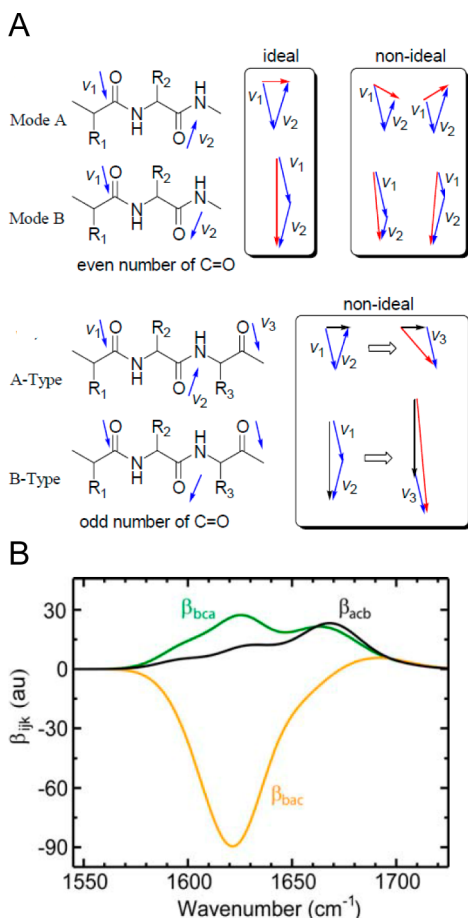**Figure 20.** (A) Ideal and nonideal A and B vibrational modes in parallel β-sheets. (B) Calculated $\beta_{bca}^{2°}$, $\beta_{bac}^{2°}$, $\beta_{acb}^{2°}$ in the amide I vibrational region.[49] Reprinted from ref 49 with permission. Copyright 2012 Elsevier.

neighboring residues. The derivatives of transition dipoles and Raman polarizability were averaged within each category, yielding the hyperpolarizability elements for amide I A and amide I B modes (Figure 20B). The calculated hyperpolarizability was used to simulate the amide I spectra of hIAPP, which were compared with the experimental data[69,70] to determine the orientation of hIAPP aggregates at the air/water interfaces, as discussed in Section 5.2.

Compared to previously reported normal-mode analyses of antiparallel β-sheet structures, the divide-and-conquer approach uniquely includes all the possible vibrational coupling amide I modes and the inhomogeneous broadening effect of amide I bands due to the presence of various amino acid side chains. This work, representing the first ab initio simulated chiral SFG spectra of macromolecules, allows for direct comparison of experimental and theoretical results to deliver orientation information on an amyloid protein at interfaces; this

information could potentially offer insights into molecular mechanism of amyloid diseases.

7.4. Comparison of Calculation Methods for Hyperpolarizability of Biomacromolecules

Due to different levels of approximation in the hyperpolarizability calculations, the three methods above have different applications in the interpretation of SFG spectra. Both Chen's and Simpson's methods compute the sum of the contributions from each monomeric unit to obtain the overall hyperpolarizability of a macromolecular structure. Chen's method is suited for vibrational modes with strong coupling between neighboring monomeric units, while Simpson's method is most useful where vibrational modes with weak coupling. Nevertheless, to quantitatively determine the extent of coupling between specific vibrational modes along a peptide backbone in various secondary structures is challenging.[133] The "divide-and-conquer" approach, on the other hand, has taken into account the vibrational coupling within the subdivided units in the macromolecular structures. With rapidly increasing computing power, it is expected that ab initio methods, when applied together with the "divide-and-conquer" approach, will become an increasingly feasible and accurate way to determine the hyperpolarizability of complex biomacromolecular systems for the purpose of simulating SFG spectra. This method will thus facilitate quantitative analyses of experimental results to furnish information about the structures and orientations of biomacromolecules at interfaces.

8. SUMMARY AND OUTLOOK

8.1. Summary

Chiral SFG is surface-specific and chiral-selective under the electric-dipole approximation and in the absence of electronic resonance for the molecular systems with a chiral interface in contact with isotropic bulk media. The surface-specificity and chiral-selectivity makes vibrational SFG spectroscopy a uniquely useful tool for probing biomacromolecules at interfaces in situ and in real time. The method is particularly powerful for probing biomacromolecules at aqueous interfaces because achiral water structures do not contribute to the background. For example, D_2O, normally used in protein vibrational studies to suppress water bending in the amide I region, is not needed; and the N−H stretch of peptide backbone can be used for characterization of protein structures without interference of the water O−H stretch. Chiral vibrational SFG spectroscopy has already been applied to the study of DNA molecules and various proteins, yielding information about the structures, orientation, and kinetics of conformational changes. It can be extended to other biomacromolecules, such as RNA, glycans, synthetic biomimetics, and chiral polymers. Although previous applications have focused on the secondary structures of single-component systems, chiral SFG should also be applicable to the study of tertiary structures and higher-order structures as well as biomacromolecular interactions, such as protein−DNA and protein−protein interactions.

8.2. Potential Applications

The unique surface-specificity and chiral-selectivity of the SFG method are expected to create research opportunities to address important problems in fundamental and engineering sciences. Examples of systems to which chiral SFG could be applied are transmembrane proteins, such as ion chan-

nels,[134,135] metabolite transporters,[136,137] and G protein-couple receptors.[138,139] These proteins transmit signals and control matter exchange across cell membranes, serving as drug targets for pharmaceutical developments. Furthermore, chiral SFG may also be used to study the amyloid aggregation associated with a number of neurodegenerative diseases, including Alzheimer's and Parkinson's diseases. More and more studies have shown that small oligomers of amyloid proteins induce membrane permeability and consequently lead to toxicity;[110–112] thus, the ability to evaluate how drug candidates alter the orientations of oligomers at membrane surfaces could potentially provide a new approach for drug discovery. Moreover, native biomacromolecules have inspired the molecular design of new classes of biomimetics and materials on the length scales of micrometers to nanometers.[126,127] Surface characterizations of these materials at ambient pressure and temperature will support the development of new materials to meet future technological needs. One of the biggest challenges in flourescent-label-free cell imaging is the overwhelming optical background from water and other biomolecules in cellular systems. The background-free nature of chiral SFG signals can potentially be utilized in the future development of vibrational imaging.[140,141] On top of that, the vibrational selectivity of chiral SFG is different from conventional SFG, IR, and Raman vibrational methods. Thus, further studies may identify subtle vibrational structures of chiral biomacromolecules, such as combination and overtone bands, which cannot be detected by conventional methods due to large spectral background. Therefore, these studies could potentially reveal new vibrational tools useful in tackling fundamental problems, such as the ultrafast dynamics of vibrational energy redistribution in complex biomacromolecules. Among these systems, photoactive biomolecular systems, e.g., light sensory receptors[142–144] and light harvesting systems,[145,146] are of particular interest. Many problems in this area are yet to be addressed owing to the limitations of conventional vibrational methods in probing complex biomacromolecular structures. For example, it remains extremely difficult to compare the efficiency of energy propagation from photoexcited chromophore to the surrounding protein backbones in α-helical structures and in β-sheet structures using conventional vibrational methods due to the lack of optically clean vibrational signals selective to the secondary structures. These kinds of questions may now be potentially tackled using the background-free vibrational signatures that can distinguish protein secondary structures provided by chiral SFG. Thus, chiral SFG could be useful in probing molecular mechanism of ultrafast dynamics of electron transfer, visual signal transduction, light harvesting, and other important photochemical processes in native biological systems.

8.3. Challenges and Outlooks

Although chiral vibrational SFG spectroscopy holds promises to address a variety of problems, at least three challenges need to be overcome for the method to solve problems of genuine biological and biomedical relevance at the fundamental level, which can be achieved in conjunction with the advancements of laser technology by the joint efforts of experimentalists and theoreticians using a multidisciplinary approach, as discussed below.

First, the temporal resolution is, thus far, limited by the signal-to-noise levels because all reported kinetic studies were carried out by monitoring the signals accumulated over time intervals on the time scales of minutes.[69,71] The temporal

resolution can extend to other time regimes by implementing advanced laser techniques. For example, the pump–probe techniques have yet been applied to chiral SFG experiments but can expand the time resolution to the nanosecond to femtosecond regimes and reveal interfacial ultrafast dynamics of biomacromolecules. Moreover, integration of two-dimensional techniques,[147–153] similar to those applied to IR spectroscopy,[107,154–156] will further enhance the selectivity of vibrational chiral SFG signals to uncover ultrafast structural dynamic details in biomacromolecular systems at interfaces. Furthermore, heterodyne detection not only allows phase measurements to disclose absolute up-versus-down molecular orientations at interfaces, it also enhances the signal levels,[72–74] making chiral SFG useful for studying a wider variety of molecular systems with improved time resolution. In addition, autocorrelation analyses of fluctuations in SFG signals can potentially extend the time scales of kinetic studies to the millisecond to microsecond regime,[157–159] the time scale on which large biomacromolecules generally undergo conformational changes. Moreover, high-resolution SFG enabled by strong and narrow bandwidth picosecond visible input in broad bandwidth spectrometers may also introduce the opportunity to study the dynamics and structures of biomacromolecules in fine vibrational details.[160] All of these technological developments will go in parallel with the advancements of laser technologies that promise more reliable, higher power, and more user-friendly light sources.

The second challenge in developing the chiral vibrational SFG method is related to the determination of hyperpolarizabilities of large biomacromolecules. Since interpretation of SFG spectra to reveal the intricacy of structures and interfacial orientations require accurate determinations of hyperpolarizability of the biomacromolecules, which rely on theoretical and computational approaches. However, computations of hyperpolarizability of large biomacromolecules under the influence of monomeric units, such as amino acids in proteins and base pairs in DNA, are demanding in terms of computational power. Thus, various approximation methods have been used to calculate hyperpolarizaibility, including coherent summation of the contributions of hyperpolarizability of monomeric units in macromolecular structures[47,48,60] and applications of the "divide-and-conquer" approach in conjunction with the ab initio methods, as discussed in section 7.[49] In applying these approximation methods, 3-dimensional structures of biomacromolecules are needed. These structures could be obtained by NMR or X-ray crystallography or molecular dynamic (MD) modeling. More sophisticated computational methods, such as quantum mechanics/molecular mechanics (QM/MM)[161,162] calculations focusing selectively on the regions of interest in biomacromolecules, such as ligand binding sites, may also be useful in analyzing functions of complex biomacromolecular systems. As computational power has become increasingly accessible at lower costs, the ab initio approach is expected to become increasingly feasible and prevalent. Thus, close collaborations between experimentalists and theoreticians are necessary to establish the SFG methods as a tool for understanding macromolecular structures and orientations at interfaces at the fundamental level.

The final challenge, a common one to almost all advanced laser spectroscopies, is to identify research problems and to prepare high-quality biological samples of genuine biological relevance. These involve corroboration of the chiral SFG methods in the cross-disciplinary research in the biological and

biomedical fields through collaborations. Moreover, techniques in molecular biology and chemical biological can be adopted in sample preparations for SFG experiments. For example, as the size of proteins increases, solid-state synthesis will no longer meet the needs. Recombinant proteins need to be expressed and purified using molecular biology methods, as exemplified by the SFG studies of recombinant GPCR rhodopsin[70] and G protein $\beta\gamma$ subunits.[163] A particular challenge associated with investigations of biomacromolecules is the anticipated complexity of the vibrational spectra. However, information specific to particular amino acids in proteins can be extracted by site-directed mutagenesis using molecular biology methods. In addition, isotopic labeling commonly used for interpreting vibrational spectra of small molecules can also be applied to biomacromolecules. For example, proteins can be expressed in cell culture grown in isotopically labeled media to produce ^{15}N or ^{13}C labeled proteins. Domains of isotopically labeled proteins can be ligated using chemical methods,[164,165] which will allow for the extraction of domain-specific information about proteins or protein complexes. Moreover, unnatural amino acids can be incorporated site-specifically into proteins using orthogonal unnatural amino acid mutagenesis.[166,167] The unnatural amino acids incorporated site-specifically into proteins can serve as vibrational spectroscopic probes[168,169] or as linkers to covalently couple to the vibrational probes. In conjunction with the use of surface platforms of live cells, colloids, suspension cell culture, nanoparticles, and microfluidic channels, these multidisciplinary approaches in chemical biology and molecular biology will change the landscape of the problems that can be accessed by the SFG methods, introducing exciting research opportunities for research into problems of biological and biomedical relevance.

AUTHOR INFORMATION

Corresponding Author

*E-mail: elsa.yan@yale.edu.

Notes

The authors declare no competing financial interest.

Biographies

Elsa Yan grew up in Hong Kong and received her B.Sc. from the Chinese University of Hong Kong. In 2000, she obtained her Ph.D. at Columbia University, working with Kenneth Eisenthal on nonlinear optics and surface sciences. From 2000-2004, she was a joint postdoctoral fellow with Richard Mathies at UC Berkeley and Thomas Sakmar at the Rockefeller University whereby she combined Raman spectroscopy with techniques in molecular biology to understand signal transduction in G-protein coupled receptor rhodopsin. In 2004,

she started working as a research assistant professor at The Rockefeller University, where she continued to develop methods in expression and purification of membrane proteins. Elsa became an Assistant Professor of Chemistry at Yale in 2007 and was promoted to Associate Professor in 2012. Her research group uses methods in spectroscopy and molecular biology to solve problems related to interactions of bioactive molecules with biomembranes.

Li Fu graduated from University of Science and Technology of China (USTC) with a bachelor's degree in chemical physics in 2008. He then joined Yale as a graduate student under the supervision of Elsa Yan, where he used sum frequency generation spectroscopy to characterize biomolecular interactions, orientation, kinetics and dynamics of proteins and membranes at interfaces. Li received his Ph.D. in biophysical chemistry in 2013 and he is currently a William Wiley Postdoctoral researcher at the Environmental Molecular Sciences Laboratory (EMSL) of Pacific Northwest National Laboratory (PNNL).
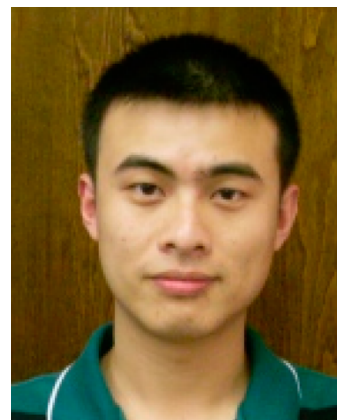
Zhuguang Wang received his B.S. in Chemical Physics from the University of Science and Technology in 2010. He then moved on to Yale University to pursue his Ph.D. in chemistry and is currently a graduate student in Elsa Yan's group. He is now applying chiral SFG spectroscopy to determine properties of biomacromolecules at interfaces. In the meantime, he is also developing SFG theories to interpret chiral SFG spectra, aiming to provide insights into the mechanisms for the biological processes at interfaces.

Wei Liu received his B.Sc. (Hons) in chemistry and economics in 2012 from the University of Miami, where he carried out undergraduate research with Prof. Roger M. Leblanc. He was recognized as the Outstanding Graduating Senior in Chemistry by the American Chemical Society South Florida Section. He joined Yale as a graduate student and is currently pursuing his Ph.D. in biophysical chemistry under the mentorship of Elsa Yan. Wei's research focuses on developing methods for characterizing biomolecules at interfaces using techniques in surface chemistry and optical spectroscopy.

REFERENCES

(1) Daniels, D. S.; Petersson, E. J.; Qiu, J. X.; Schepartz, A. *J. Am. Chem. Soc.* **2007**, *129*, 1532.

(2) Appella, D. H.; Christianson, L. A.; Karle, I. L.; Powell, D. R.; Gellman, S. H. *J. Am. Chem. Soc.* **1996**, *118*, 13071.

(3) Simon, R. J.; Kania, R. S.; Zuckermann, R. N.; Huebner, V. D.; Jewell, D. A.; Banville, S.; Ng, S.; Wang, L.; Rosenberg, S.; Marlowe, C. K. *Proc. Natl. Acad. Sci. U.S.A.* **1992**, *89*, 9367.

(4) Ji, N.; Shen, Y.-R. *J. Am. Chem. Soc.* **2004**, *126*, 15008.

(5) Ji, N.; Ostroverkhov, V.; Belkin, M.; Shiu, Y.-J.; Shen, Y.-R. *J. Am. Chem. Soc.* **2006**, *128*, 8845.

(6) Wei, F.; Xu, Y.-y.; Guo, Y.; Liu, S.-l.; Wang, H.-f. *Chin. J. Chem. Phys.* **2009**, *22*, 592.

(7) Fischer, P.; Hache, F. *Chirality* **2005**, *17*, 421.

(8) Cheon, S.; Lee, H.; Choi, J. H.; Cho, M. *J. Chem. Phys.* **2007**, *126*.

(9) Richmond, G. L. *Anal. Chem.* **1997**, *69*, A536.

(10) Messmer, M. C.; Conboy, J. C.; Richmond, G. L. *J. Am. Chem. Soc.* **1995**, *117*, 8039.

(11) Wang, J.; Chen, C.; Buck, S. M.; Chen, Z. *J. Phys. Chem. B* **2001**, *105*, 12118.

(12) Weidner, T.; Apte, J. S.; Gamble, L. J.; Castner, D. G. *Langmuir* **2010**, *26*, 3433.

(13) Kim, J.; Somorjai, G. A. *J. Am. Chem. Soc.* **2003**, *125*, 3150.

(14) Liu, Y.; Jasensky, J.; Chen, Z. *Langmuir* **2011**, *28*, 2113.

(15) Zhang, C.; Myers, J. N.; Chen, Z. *Soft Matter* **2013**.

(16) Shen, Y. *Nature* **1989**, *337*, 519.

(17) Eisenthal, K. *Chem. Rev.* **1996**, *96*, 1343.

(18) Wang, H. F.; Gan, W.; Lu, R.; Rao, Y.; Wu, B. H. *Int. Rev. Phys. Chem.* **2005**, *24*, 191.

(19) Richmond, G. *Chem. Rev.* **2002**, *102*, 2693.

(20) Shen, Y.-R. *The Principles of Nonlinear Optics*; Wiley-Interscience: New York, 1984; p 576.

(21) Boyed, R. W. *Nonlinear Opt.*; Academic Press: New York, 2003; p 578.

(22) Lambert, A. G.; Davies, P. B.; Neivandt, D. J. *Appl. Spectrosc. Rev.* **2005**, *40*, 103.

(23) Simpson, G. J. *ChemPhysChem* **2004**, *5*, 1301.

(24) Haupert, L. M.; Simpson, G. J. *Annu. Rev. Phys. Chem.* **2009**, *60*, 345.

(25) Petralli-Mallow, T.; Wong, T.; Byers, J.; Yee, H.; Hicks, J. *J. Phys. Chem.* **1993**, *97*, 1383.

(26) Zyss, J.; Nicoud, J.; Coquillay, M. *J. Chem. Phys.* **1984**, *81*, 4160.

(27) Roke, S. *ChemPhysChem* **2009**, *10*, 1380.

(28) Moore, F.; Richmond, G. *Acc. Chem. Res.* **2008**, *41*, 739.

(29) Zhuang, X.; Miranda, P.; Kim, D.; Shen, Y. *Phys. Rev. B* **1999**, *59*, 12632.

(30) Sung, W.; Seok, S.; Kim, D.; Tian, C.; Shen, Y. *Langmuir* **2010**, *26*, 18266.

(31) Chen, Z.; Shen, Y. R.; Somorjai, G. A. *Annu. Rev. Phys. Chem.* **2002**, *53*, 437.

(32) Cremer, P. S.; Su, X. C.; Shen, Y. R.; Somorjai, G. A. *J. Am. Chem. Soc.* **1996**, *118*, 2942.

(33) Lahann, J.; Mitragotri, S.; Tran, T. N.; Kaido, H.; Sundaram, J.; Choi, I. S.; Hoffer, S.; Somorjai, G. A.; Langer, R. *Science* **2003**, *299*, 371.

(34) Bain, C. D.; Davies, P. B.; Ong, T. H.; Ward, R. N.; Brown, M. A. *Langmuir* **1991**, *7*, 1563.

(35) Somorjai, G. A.; Frei, H.; Park, J. Y. *J. Am. Chem. Soc.* **2009**, *131*, 16589.

(36) Nakayama, Y.; Pauzauskie, P. J.; Radenovic, A.; Onorato, R. M.; Saykally, R. J.; Liphardt, J.; Yang, P. D. *Nature* **2007**, *447*, 1098.

(37) Phillips, D. C.; York, R. L.; Mermut, O.; McCrea, K. R.; Ward, R. S.; Somorjai, G. A. *J. Phys. Chem. C* **2007**, *111*, 255.

(38) Shen, Y. R.; Ostroverkhov, V. *Chem. Rev.* **2006**, *106*, 1140.

(39) Richmond, G. *Annu. Rev. Phys. Chem.* **2001**, *52*, 357.

(40) Miranda, P.; Xu, L.; Shen, Y.; Salmeron, M. *Phys. Rev. Lett.* **1998**, *81*, 5876.

(41) Sovago, M.; Campen, R. K.; Bakker, H. J.; Bonn, M. *Chem. Phys. Lett.* **2009**, *470*, 7.

(42) McGuire, J. A.; Shen, Y. R. *Science* **2006**, *313*, 1945.

(43) Arnolds, H.; Bonn, M. *Surf. Sci. Rep.* **2010**, *65*, 45.

(44) Moad, A. J.; Simpson, G. J. *J. Phys. Chem. B* **2004**, *108*, 3548.

(45) Fu, L.; Wang, Z.; Yan, E. C. Y. *Int. J. Mol. Sci.* **2011**, *12*, 9404.

(46) Roy, S.; Hung, K. K.; Stege, U.; Hore, D. K. *Appl. Spectrosc. Rev.* **2014**, *49*, 233.

(47) Perry, J. M.; Moad, A. J.; Begue, N. J.; Wampler, R. D.; Simpson, G. J. *J. Phys. Chem. B* **2005**, *109*, 20009.

(48) Nguyen, K. T.; King, J. T.; Chen, Z. *J. Phys. Chem. B* **2010**, *114*, 8291.

(49) Xiao, D.; Fu, L.; Liu, J.; Batista, V. S.; Yan, E. C. Y. *J. Mol. Biol.* **2012**, *421*, 537.

(50) Simpson, G. J.; Dailey, C. A.; Plocinik, R. M.; Moad, A. J.; Polizzi, M. A.; Everly, R. M. *Anal. Chem.* **2005**, *77*, 215.

(51) Belkin, M.; Kulakov, T.; Ernst, K.; Yan, L.; Shen, Y. *Phys. Rev. Lett.* **2000**, *85*, 4474.

(52) Liu, F. C. *J. Phys. Chem.* **1991**, *95*, 7180.

(53) Liu, J.; Conboy, J. C. *J. Am. Chem. Soc.* **2004**, *126*, 8376.

(54) Brown, K. L.; Conboy, J. C. *J. Phys. Chem. B* **2013**, *117*, 15041.

(55) Holman, J.; Davies, P. B.; Nishida, T.; Ye, S.; Neivandt, D. J. *J. Phys. Chem. B* **2005**, *109*, 18723.

(56) Nishida, T.; Johnson, C. M.; Holman, J.; Osawa, M.; Davies, P. B.; Ye, S. *Phys. Rev. Lett.* **2006**, *96*, 077402.

(57) Liu, W.; Wang, Z.; Fu, L.; Leblanc, R. M.; Yan, E. C. *Langmuir* **2013**, *29*, 15022.

(58) Marsh, D. *Biophys. J.* **1997**, *72*, 2710.

(59) Tsuboi, M.; Ikeda, T.; Ueda, T. *J. Raman Spectrosc.* **1991**, *22*, 619.

(60) Nguyen, K. T.; Le Clair, S. V.; Ye, S. J.; Chen, Z. *J. Phys. Chem. B* **2009**, *113*, 12169.

(61) Wang, J.; Clarke, M. L.; Chen, Z. *Anal. Chem.* **2004**, *76*, 2159.

(62) Stokes, G. Y.; Gibbs-Davis, J. M.; Boman, F. C.; Stepp, B. R.; Condie, A. G.; Nguyen, S. T.; Geiger, F. M. *J. Am. Chem. Soc.* **2007**, *129*, 7492.

(63) Hore, D. K.; King, J. L.; Moore, F. G.; Alavi, D. S.; Hamamoto, M. Y.; Richmond, G. L. *Appl. Spectrosc.* **2004**, *58*, 1377.

(64) Richter, L. J.; Petralli-Mallow, T. P.; Stephenson, J. C. *Opt. Lett.* **1998**, *23*, 1594.

(65) McGuire, J.; Beck, W.; Wei, X.; Shen, Y. *Opt. Lett.* **1999**, *24*, 1877.

(66) Van Der Ham, E.; Vrehen, Q.; Eliel, E. *Opt. Lett.* **1996**, *21*, 1448.

(67) Ma, G.; Liu, J.; Fu, L.; Yan, E. C. Y. *Appl. Spectrosc.* **2009**, *63*, 528.

(68) Isaienko, O.; Borguet, E. *Opt. Express.* **2012**, *20*, 547.

(69) Fu, L.; Ma, G.; Yan, E. C. Y. *J. Am. Chem. Soc.* **2010**, *132*, 5405.

(70) Fu, L.; Liu, J.; Yan, E. C. Y. *J. Am. Chem. Soc.* **2011**, *133*, 8094.

(71) Wang, Z.; Fu, L.; Yan, E. C. Y. *Langmuir* **2013**, *29*, 4077.

(72) Stiopkin, I. V.; Jayathilake, H. D.; Bordenyuk, A. N.; Benderskii, A. V. *J. Am. Chem. Soc.* **2008**, *130*, 2271.

(73) Nihonyanagi, S.; Yamaguchi, S.; Tahara, T. *J. Chem. Phys.* **2009**, *130*, 204704.

(74) Covert, P. A.; FitzGerald, W. R.; Hore, D. K. *J. Chem. Phys.* **2012**, *137*, 014201.

(75) Kim, J.; Kim, G.; Cremer, P. S. *Langmuir* **2001**, *17*, 7255.

(76) Roke, S.; Schins, J.; Muller, M.; Bonn, M. *Phys. Rev. Lett.* **2003**, *90*, 128101.

(77) Bonn, M.; Roke, S.; Berg, O.; Juurlink, L. B.; Stamouli, A.; Müller, M. *J. Phys. Chem. B* **2004**, *108*, 19083.

(78) Ma, G.; Allen, H. C. *Langmuir* **2006**, *22*, 5341.

(79) Chen, C.; Zhu, S.-F.; Liu, B.; Wang, L.-X.; Zhou, Q.-L. *J. Am. Chem. Soc.* **2007**, *129*, 12616.

(80) Wurpel, G. W. H.; Sovago, M.; Bonn, M. *J. Am. Chem. Soc.* **2007**, *129*, 8420.

(81) Chen, X.; Wang, J.; Sniadecki, J. J.; Even, M. A.; Chen, Z. *Langmuir* **2005**, *21*, 2662.

(82) Wang, J.; Even, M. A.; Chen, X.; Schmaier, A. H.; Waite, J. H.; Chen, Z. *J. Am. Chem. Soc.* **2003**, *125*, 9914.

(83) vandenAkker, C. C.; Engel, M. F. M.; Velikov, K. P.; Bonn, M.; Koenderink, G. H. *J. Am. Chem. Soc.* **2011**, *133*, 18030.

(84) Fu, L.; Xiao, D.; Wang, Z.; Batista, V. S.; Yan, E. C. Y. *J. Am. Chem. Soc.* **2013**, *135*, 3592.

(85) Conboy, J. C.; Messmer, M. C.; Richmond, G. L. *J. Phys. Chem.* **1996**, *100*, 7617.

(86) Diesner, M.-O.; Howell, C.; Kurz, V.; Verreault, D.; Koelsch, P. *J. Phys. Chem. Lett.* **2010**, *1*, 2339.

(87) Holden, M. A.; Cremer, P. S. *Annu. Rev. Phys. Chem.* **2005**, *56*, 369.

(88) Castellana, E. T.; Cremer, P. S. *Surf. Sci. Rep.* **2006**, *61*, 429.

(89) White, R. J.; Zhang, B.; Daniel, S.; Tang, J. M.; Ervin, E. N.; Cremer, P. S.; White, H. S. *Langmuir* **2006**, *22*, 10777.

(90) Roke, S.; Gonella, G. *Annu. Rev. Phys. Chem.* **2012**, *63*, 353.

(91) Wang, H.; Yan, E. C. Y.; Borguet, E.; Eisenthal, K. *Chem. Phys. Lett.* **1996**, *259*, 15.

(92) Eisenthal, K. B. *Chem. Rev.* **2006**, *106*, 1462.

(93) de Aguiar, H. B.; Strader, M. L.; de Beer, A. G.; Roke, S. *J. Phys. Chem. B* **2011**, *115*, 2970.

(94) Yan, E. C. Y.; Liu, Y.; Eisenthal, K. B. *J. Phys. Chem. B* **1998**, *102*, 6331.

(95) Srivastava, A.; Eisenthal, K. B. *Chem. Phys. Lett.* **1998**, *292*, 345.

(96) Yan, E. C. Y.; Eisenthal, K. B. *Biophys. J.* **2000**, *79*, 898.

(97) Zeng, J.; Eckenrode, H. M.; Dounce, S. M.; Dai, H.-L. *Biophys. J.* **2013**, *104*, 139.

(98) de Beer, A. G.; Roke, S. *Phys. Rev. B* **2007**, *75*, 245438.

(99) Wang, J.; Chen, X.; Clarke, M. L.; Chen, Z. *Proc. Natl. Acad. Sci. U.S.A.* **2005**, *102*, 4978.

(100) Boughton, A. P.; Nguyen, K.; Andricioaei, I.; Chen, Z. *Langmuir* **2011**, *27*, 14343.

(101) Walter, S. R.; Geiger, F. M. *J. Phys. Chem. Lett.* **2009**, *1*, 9.

(102) Degrado, W. F.; Lear, J. D. *J. Am. Chem. Soc.* **1985**, *107*, 7684.

(103) Mink, J.; Keresztury, G.; Kristóf, J.; Mihály, J. *Interfacial Science in Ceramic Joining*; Springer: New York, 1998; p 480.

(104) Mirkin, N. G.; Krimm, S. *J. Phys. Chem. A* **2004**, *108*, 5438.

(105) Rocha-Mendoza, I.; Yankelevich, D. R.; Wang, M.; Reiser, K. M.; Frank, C. W.; Knoesen, A. *Biophys. J.* **2007**, *93*, 4433.

(106) Nagahara, T.; Kisoda, K.; Harima, H.; Aida, M.; Ishibashi, T.-a. *J. Phys. Chem. B* **2009**, *113*, 5098.

(107) Shim, S. H.; Strasfeld, D. B.; Ling, Y. L.; Zanni, M. T. *Proc. Natl. Acad. Sci. U.S.A.* **2007**, *104*, 14197.

(108) Strasfeld, D. B.; Ling, Y. L.; Shim, S. H.; Zanni, M. T. *J. Am. Chem. Soc.* **2008**, *130*, 6698.

(109) Strasfeld, D. B.; Ling, Y. L.; Gupta, R.; Raleigh, D. P.; Zanni, M. T. *J. Phys. Chem. B* **2009**, *113*, 15679.

(110) Jayasinghe, S. A.; Langen, R. *Biochim. Biophys. Acta.-Biomembranes* **2007**, *1768*, 2002.

(111) Engel, M. F. M. *Chem. Phys. Lipids* **2009**, *160*, 1.

(112) Friedman, R.; Pellarin, R.; Caflisch, A. *J. Mol. Biol.* **2009**, *387*, 407.

(113) Luca, S.; Yau, W. M.; Leapman, R.; Tycko, R. *Biochemistry* **2007**, *46*, 13505.

(114) Knight, J. D.; Hebda, J. A.; Miranker, A. D. *Biochemistry* **2006**, *45*, 9496.

(115) Jayasinghe, S. A.; Langen, R. *Biochemistry* **2005**, *44*, 12113.

(116) Eichner, T.; Radford, S. E. *Mol. Cell* **2011**, *43*, 8.

(117) Janson, J.; Ashley, R. H.; Harrison, D.; McIntyre, S.; Butler, P. C. *Diabetes* **1999**, *48*, 491.

(118) Hoppener, J. W. M.; Ahren, B.; Lips, C. J. M. *N. Engl. J. Med.* **2000**, *343*, 411.

(119) Chiti, F.; Dobson, C. M. *Annu. Rev. Biochem.* **2006**, *75*, 333.

(120) Englander, S. W. *Annu. Rev. Biophys. Biomol. Struct.* **2000**, *29*, 213.

(121) Tobler, S. A.; Fernandez, E. J. *Protein Sci.* **2002**, *11*, 1340.

(122) Lu, X.; Wintrode, P. L.; Surewicz, W. K. *Proc. Natl. Acad. Sci. U.S.A.* **2007**, *104*, 1510.

(123) Paterson, Y.; Englander, S. W.; Roder, H. *Science* **1990**, *249*, 755.

(124) Powell, K. D.; Ghaemmaghami, S.; Wang, M. Z.; Ma, L.; Oas, T. G.; Fitzgerald, M. C. *J. Am. Chem. Soc.* **2002**, *124*, 10256.

(125) Madey, T. E.; Yates, J. T., Jr *Vibrational Spectroscopy of Molecules on Surfaces*; Springer: New York, 1987; p 484.

(126) Lehn, J. M. *Angew. Chem., Int. Ed. Engl.* **1988**, *27*, 89.

(127) Zhang, S. G. *Nat. Biotechnol.* **2003**, *21*, 1171.

(128) Roy, S.; Naka, T. L.; Hore, D. K. *J. Phys. Chem. C* **2013**, *117*, 24955.

(129) Hall, S. A.; Jena, K. C.; Trudeau, T. G.; Hore, D. K. *J. Phys. Chem. C* **2011**, *115*, 11216.

(130) Volkov, V.; Bonn, M. *J. Phys. Chem. B* **2013**.

(131) Roeters, S. J.; van Dijk, C. N.; Torres-Knoop, A.; Backus, E. H. G.; Campen, R. K.; Bonn, M.; Woutersen, S. *J. Phys. Chem. A* **2013**, *117*, 6311.

(132) Marsh, D.; Müller, M.; Schmitt, F.-J. *Biophys. J.* **2000**, *78*, 2499.

(133) Hayashi, T.; Mukamel, S. *J. Phys. Chem. B* **2007**, *111*, 11032.

(134) Gouaux, E.; MacKinnon, R. *Science* **2005**, *310*, 1461.

(135) Doyle, D. A.; Cabral, J. M.; Pfuetzner, R. A.; Kuo, A. L.; Gulbis, J. M.; Cohen, S. L.; Chait, B. T.; MacKinnon, R. *Science* **1998**, *280*, 69.

(136) Merianos, H. J.; Cadieux, N.; Lin, C. H.; Kadner, R. J.; Cafiso, D. S. *Nat. Struct. Biol.* **2000**, *7*, 205.

(137) Borst, P.; Elferink, R. O. *Annu. Rev. Biochem.* **2002**, *71*, 537.

(138) Rosenbaum, D. M.; Rasmussen, S. G. F.; Kobilka, B. K. *Nature* **2009**, *459*, 356.

(139) Pierce, K. L.; Premont, R. T.; Lefkowitz, R. J. *Nat. Rev. Mol. Cell Biol.* **2002**, *3*, 639.

(140) Ji, N.; Zhang, K.; Yang, H.; Shen, Y. R. *J. Am. Chem. Soc.* **2006**, *128*, 3482.

(141) Cimatu, K.; Baldelli, S. *J. Am. Chem. Soc.* **2008**, *130*, 8030.

(142) Luecke, H.; Schobert, B.; Richter, H. T.; Cartailler, J. P.; Lanyi, J. K. *J. Mol. Biol.* **1999**, *291*, 899.

(143) Menon, S. T.; Han, M.; Sakmar, T. P. *Physiol. Rev.* **2001**, *81*, 1659.

(144) Palczewski, K.; Kumasaka, T.; Hori, T.; Behnke, C. A.; Motoshima, H.; Fox, B. A.; Le Trong, I.; Teller, D. C.; Okada, T.; Stenkamp, R. E.; Yamamoto, M.; Miyano, M. *Science* **2000**, *289*, 739.

(145) McEvoy, J. P.; Brudvig, G. W. *Chem. Rev.* **2006**, *106*, 4455.

(146) Umena, Y.; Kawakami, K.; Shen, J. R.; Kamiya, N. *Nature* **2011**, *473*, 55.

(147) Ni, Y. C.; Gruenbaum, S. M.; Skinner, J. L. *Proc. Natl. Acad. Sci. U.S.A.* **2013**, *110*, 1992.

(148) Singh, P. C.; Nihonyanagi, S.; Yamaguchi, S.; Tahara, T. *J. Chem. Phys.* **2013**, *139*, 161101.

(149) Xiong, W.; Laaser, J. E.; Mehlenbacher, R. D.; Zanni, M. T. *Proc. Natl. Acad. Sci. U. S. A.* **2011**, *108*, 20902.

(150) Carter, J. A.; Wang, Z. H.; Dlott, D. D. *Acc. Chem. Res.* **2009**, *42*, 1343.

(151) Li, Q.; Hua, R.; Chou, K. C. *J. Phys. Chem. B* **2008**, *112*, 2315.

(152) Cho, M. H. *J. Chem. Phys.* **2000**, *112*, 9978.

(153) Bredenbeck, J.; Ghosh, A.; Nienhuys, H. K.; Bonn, M. *Acc. Chem. Res.* **2009**, *42*, 1332.

(154) Ganim, Z.; Chung, H. S.; Smith, A. W.; Deflores, L. P.; Jones, K. C.; Tokmakoff, A. *Acc. Chem. Res.* **2008**, *41*, 432.

(155) Hamm, P.; Lim, M.; DeGrado, W. F.; Hochstrasser, R. M. *Proc. Natl. Acad. Sci. U.S.A.* **1999**, *96*, 2036.

(156) Kwac, K.; Cho, M. H. *J. Chem. Phys.* **2003**, *119*, 2256.

(157) Yan, E. C. Y.; Eisenthal, K. B. *J. Phys. Chem. B* **2000**, *104*, 6686.

(158) Sly, K. L.; Mok, S. W.; Conboy, J. C. *Anal. Chem.* **2013**, *85*, 8429.

(159) Zhao, X. L.; Eisenthal, K. B. *J. Chem. Phys.* **1995**, *102*, 5818.

(160) Velarde, L.; Zhang, X. Y.; Lu, Z.; Joly, A. G.; Wang, Z. M.; Wang, H. F. *J. Chem. Phys.* **2011**, *135*, 241102.

(161) Senn, H. M.; Thiel, W. *Angew. Chem., Int. Ed.* **2009**, *48*, 1198.

(162) Sproviero, E. M.; Gascon, J. A.; McEvoy, J. P.; Brudvig, G. W.; Batista, V. S. *J. Am. Chem. Soc.* **2008**, *130*, 3428.

(163) Chen, X. Y.; Boughton, A. P.; Tesmer, J. J. G.; Chen, Z. *J. Am. Chem. Soc.* **2007**, *129*, 12658.

(164) Muir, T. W. *Annu. Rev. Biochem.* **2003**, *72*, 249.

(165) Chen, G.; Wan, Q.; Tan, Z. P.; Kan, C.; Hua, Z. H.; Ranganathan, K.; Danishefsky, S. J. *Angew. Chem., Int. Ed.* **2007**, *46*, 7383.

(166) Liu, C. C.; Schultz, P. G. *Annu. Rev. Biochem.* **2010**, *79*, 413.

(167) Ye, S. X.; Kohrer, C.; Huber, T.; Kazmi, M.; Sachdev, P.; Yan, E. C. Y.; Bhagat, A.; RajBhandary, U. L.; Sakmar, T. P. *J. Biol. Chem.* **2008**, *283*, 1525.

(168) Ye, S. X.; Zaitseva, E.; Caltabiano, G.; Schertler, G. F. X.; Sakmar, T. P.; Deupi, X.; Vogel, R. *Nature* **2010**, *464*, 1386.

(169) Schultz, K. C.; Supekova, L.; Ryu, Y. H.; Xie, J. M.; Perera, R.; Schultz, P. G. *J. Am. Chem. Soc.* **2006**, *128*, 13984.

NOTE ADDED AFTER ASAP PUBLICATION

This paper was published to the Web on May 2, 2014, with errors in equations 4 and 12. These were corrected in the version published on June 10, 2014.

8498

dx.doi.org/10.1021/cr4006044 | *Chem. Rev.* 2014, 114, 8471−8498